

Cosmic Shear Measurements with DES Science Verification Data

M. R. Becker^{*1,2}, M. A. Troxel³, N. MacCrann³, E. Krause², T. F. Eifler^{4,5}, O. Friedrich^{6,7}, A. Nicola⁸, A. Refregier⁸, A. Amara⁸, D. Bacon⁹, G. M. Bernstein⁴, C. Bonnett¹⁰, S. L. Bridle³, M. T. Busha^{1,2}, C. Chang⁸, S. Dodelson^{11,12}, B. Erickson¹³, A. E. Evrard^{14,13}, J. Frieman^{11,12}, E. Gaztanaga¹⁵, D. Gruen^{6,7}, W. Hartley⁸, B. Jain⁴, M. Jarvis⁴, T. Kacprzak⁸, D. Kirk¹⁶, A. Kravtsov¹², B. Leistedt¹⁶, E. S. Rykoff^{2,17}, C. Sabiu¹⁸, C. Sánchez¹⁰, H. Seo¹⁹, E. Sheldon²⁰, R. H. Wechsler^{1,2,17}, J. Zuntz³, T. Abbott²¹, F. B. Abdalla¹⁶, S. Allam¹¹, R. Armstrong²², M. Banerji^{23,24}, A. H. Bauer¹⁵, A. Benoit-Lévy¹⁶, E. Bertin^{25,26}, D. Brooks¹⁶, E. Buckley-Geer¹¹, D. L. Burke^{2,17}, D. Capozzi⁹, A. Carnero Rosell^{27,28}, M. Carrasco Kind^{29,30}, J. Carretero^{15,10}, F. J. Castander¹⁵, M. Crocce¹⁵, C. E. Cunha², C. B. D’Andrea⁹, L. N. da Costa^{27,28}, D. L. DePoy³¹, S. Desai^{32,33}, H. T. Diehl¹¹, J. P. Dietrich^{32,7}, P. Doel¹⁶, A. Fausti Neto²⁷, E. Fernandez¹⁰, D. A. Finley¹¹, B. Flaugher¹¹, P. Fosalba¹⁵, D. W. Gerdes¹³, R. A. Gruendl^{29,30}, G. Gutierrez¹¹, K. Honscheid^{34,19}, D. J. James²¹, K. Kuehn³⁵, N. Kuropatkin¹¹, O. Lahav¹⁶, T. S. Li³¹, M. Lima^{36,27}, M. A. G. Maia^{27,28}, M. March⁴, P. Martini^{34,37}, P. Melchior^{34,19}, C. J. Miller^{14,13}, R. Miquel^{10,38}, J. J. Mohr^{32,33,6}, R. C. Nichol⁹, B. Nord¹¹, R. Ogando^{27,28}, A. A. Plazas⁵, K. Reil^{2,17}, A. K. Romer³⁹, A. Roodman^{2,17}, M. Sako⁴, E. Sanchez⁴⁰, V. Scarpine¹¹, M. Schubnell¹³, I. Sevilla-Noarbe^{40,29}, R. C. Smith²¹, M. Soares-Santos¹¹, F. Sobreira^{11,27}, E. Suchyta^{34,19}, M. E. C. Swanson³⁰, G. Tarle¹³, J. Thaler⁴¹, D. Thomas^{9,42}, V. Vikram⁴³, A. R. Walker²¹

(The DES Collaboration)

Affiliations are listed at the end of the paper

ABSTRACT

We present measurements of weak gravitational lensing cosmic shear two-point statistics using Dark Energy Survey Science Verification data. We demonstrate that our results are robust to the choice of shear measurement pipeline, either NGMIX or IM3SHAPE, and robust to the choice of two-point statistic, including both real and Fourier-space statistics. Our results pass a suite of null tests including tests for B-mode contamination and direct tests for any dependence of the two-point functions on a set of 16 observing conditions and galaxy properties, such as seeing, airmass, galaxy color, galaxy magnitude, etc. We furthermore use a large suite of simulations to compute the covariance matrix of the cosmic shear measurements and assign statistical significance to our null tests. We find that our covariance matrix is consistent with the halo model prediction, indicating that it has the appropriate level of halo sample variance. We compare the same jackknife procedure applied to the data and the simulations in order to search for additional sources of noise not captured by the simulations. We find no statistically significant extra sources of noise in the data. The overall detection significance with tomography for our highest source density catalog is 9.7σ . Cosmological constraints from the measurements in this work are presented in a companion paper (DES et al. 2015).

Key words: gravitational lensing: weak; methods: data analysis

1 INTRODUCTION

Cosmic shear, the weak gravitational lensing of galaxies due to large-scale structure, is one of the most statistically pow-

* Corresponding author: beckermr@stanford.edu

erful probes of Dark Energy, massive neutrinos, and potential modifications to General Relativity (Albrecht et al. 2006; Peacock & Schneider 2006). Due to its powerful potential as a cosmological probe, many ongoing and future surveys (KIlo-Degree Survey: KIDS¹, Hyper Suprime-Cam survey: HSC², the Dark Energy Survey: DES³, the Large Synoptic Survey Telescope: LSST⁴, Euclid⁵ and WFIRST⁶) will employ cosmic shear as one of their principle cosmological probes. Cosmic shear two-point measurements, in their simplest form, are made by correlating the shapes of many millions of galaxies as a function of their separation in angle. Additionally, if the galaxies can be separated as a function of redshift, then tomographic cosmic shear measurements can be made by cross-correlating galaxies at different redshifts, which can probe the evolution of large-scale structure. The galaxies themselves have intrinsic shapes that are an order of magnitude larger than the cosmic shear signal, which means that cosmic shear measurements involve extracting small correlations from a large, shape noise-dominated background. Competitive cosmological constraints from cosmic shear will require of order percent level or better measurements at all steps of the analysis, from shear measurement to the measurements of cosmic shear two-point functions (see, e.g., Weinberg et al. 2013 or Kilbinger 2014 for a review).

Cosmic shear was first detected in 2000 (Bacon et al. 2000; Kaiser et al. 2000; Wittman et al. 2000; van Waerbeke et al. 2000). The most recent results have detected correlated shapes on scales from a few to 60 arcminutes from the Deep Lens Survey (Jee et al. 2013), the Sloan Digital Sky Survey (Lin et al. 2012; Huff et al. 2014) and the Canada-France-Hawaii Legacy Survey (Kilbinger et al. 2013), including in 6 redshift bins (Heymans et al. 2013). Future cosmic shear measurements will be very high signal-to-noise and over much larger survey areas, yielding a wealth of cosmological information.

Cosmic shear measurements are challenging for a variety of reasons. First and foremost, shear measurements are subject to biases that can arise from a number of sources. These biases are usually split into additive and multiplicative components. Sources of additive biases include inaccuracies in the modeling of the point spread function (PSF), inaccuracies in correcting for the effect of the PSF on galaxy images, astrometric errors, and contaminating flux from nearby galaxies. Multiplicative biases can arise from the effects of noise on the shear measurement process, incorrect estimates of the size of the PSF, and, for model-fitting methods, mismatches between an object's true underlying structure and the model employed in the shear measurement process. Additionally, many modern shear measurement methods require accurate estimates of the distribution of galaxy shapes and profiles in the absence of lensing to either serve as priors in the extraction of shapes from the data or to directly make corrections to the data. These priors can be estimated from high-resolution *Hubble Space Telescope* imaging, but

must be matched to the observational sample under consideration.

Significant computational and scientific challenges in cosmic shear measurements remain, even in the presence of perfect shear measurements. The cosmic shear field is the result of lensing by the non-linearly evolved matter density field. Accurate predictions for the non-linear matter power spectrum, even just for pure dark matter models, are computationally expensive and are needed at every point in parameter space in order to extract cosmological parameters. Emulators, like the Coyote Universe (Heitmann et al. 2014), have solved this problem for typical cosmologies and Dark Energy models, but neglect important physical effects, like galaxy formation, on the matter power spectrum. Additionally, some physical effects of galaxy formation break the assumption that galaxies are randomly oriented in the absence of lensing. These effects, called intrinsic alignments, can introduce correlations in the shapes of galaxies that are not due to lensing, complicating the interpretation of cosmic shear measurements (see, e.g., Troxel & Ishak 2015; Kirk et al. 2015). Furthermore, even if the mean signal can be modeled properly, the covariance matrix of cosmic measurements is dominated by sample variance, requiring either extensive suites of numerical simulations or complicated halo model calculations. The (mis-)estimation of photometric redshifts (photo-zs) from imaging data is yet another important source of bias in the modeling of cosmic shear measurements. Finally, for precise cosmic shear measurements, lensing magnification, second-order lensing effects, and source selection effects will be important.

In this work, we present cosmic shear measurements from Dark Energy Survey (DES) Science Verification (SV) data (Gruendl et al. in preparation; Rykoff et al. in preparation) using the shear catalogs by Jarvis et al. (2015). We employ a combination of two shear estimation codes and two photometric redshift estimation codes, each of which takes a different approach to many of the issues described above. Additionally, we use a suite of ray-traced weak lensing simulations to compute the sample variance contributions to the covariance matrix of our measurements. We then present an extensive suite of tests of both the signals in the data and the covariance matrices. These tests include comparisons of the covariance matrices to halo model predictions, null tests of B-mode contamination, and null tests based on comparing the signal between halves of the source galaxy sample split by survey metadata, like seeing, depth, etc. Overall, we find no statistically significant contamination. This paper is closely related to three other papers, namely the presentation of the DES SV shear catalog (Jarvis et al. 2015), the presentation of the DES SV photometric redshifts for weak lensing (Bonnett et al. 2015), and a companion paper that presents constraints on cosmological parameters using the measurements in this paper (DES et al. 2015).

This work is organized as follows. In Section 2, we describe the DES SV shear catalogs and photometric redshifts. Then we describe the mock catalogs used in this work in Section 3. Next, in Section 4, we present our detections of cosmic shear with DES SV data and our real-space two-point function estimators. Appendix A describes alternate two-point estimators besides the real-space correlation functions used for the bulk of this work. We discuss the estimation and validation of our covariance estimation in Section 5. Then, we

¹ <http://kids.strw.leidenuniv.nl/>

² <http://www.naoj.org/Projects/HSC/HSCProject.html>

³ <http://www.darkenergysurvey.org>

⁴ <http://www.lsst.org>

⁵ <http://sci.esa.int/euclid>

⁶ <http://wfirst.gsfc.nasa.gov>

describe our suite of null and consistency tests of our measurements in Section 6. Finally, we conclude in Section 7. The shear correlation functions and simulation covariance matrices from this work are available as online supplementary material with this paper.

2 DATA

The DES SV data with weak lensing measurements consists of 139 square degrees of five-band imaging with roughly 7 exposures per band on average (Diehl 2012; Flaugher et al. 2012; Honscheid et al. 2012; Flaugher et al. 2015). The depth of the data is somewhat shallower than the expected ~ 10 -exposure average depth of the DES five-year data. The basic reductions and co-add source detection were done with the DES data management (DESDM) system as described in Desai et al. (2012) and Gruendl et al. (in preparation). We use the shear measurements from Jarvis et al. (2015) performed on the DES SV Gold sample of galaxies (Rykoff et al., in preparation). For more information on the shear measurements and recommended cuts, we refer the reader to Jarvis et al. (2015). The shear measurement pipelines and photo-zs used in this work are described below for completeness. We use the “reduced shear” ellipticity definition (Schneider & Seitz 1995). Finally, note that the two shear measurement codes used in this work are not identical, employing different cuts and different parts of the DES SV data. Thus they have overall source number densities and photometric redshift distributions. These differences, which we expect to be smaller in future DES analyses (see Jarvis et al. 2015), have no effect on the major conclusions of this work and are in fact important in verifying the robustness of our results.

2.1 Shear Measurement Pipeline 1: ngmix

The NGMIX⁷ pipeline (Sheldon 2014) uses sums of Gaussians to represent simple galaxy models (Hogg & Lang 2013). The model parameters of each object are sampled using Markov Chain Monte Carlo (MCMC) techniques applied to a full likelihood which forward models the galaxy and its convolution with the PSF. The total likelihood for each object is a product of the likelihoods of the individual images of each object. The r -, i - and z -bands are fit simultaneously with the same model shape, but different amplitudes. The samples of the likelihood are then used with the `lensfit` algorithm (Miller et al. 2007) to measure the shear of each object using a prior on the intrinsic distribution of shapes from the GREAT3 (Mandelbaum et al. 2014) release of the COSMOS galaxy sample. The final effective source number density of the NGMIX catalog is $\simeq 6.1$ galaxies per square arcminute.⁸ Each source has an associated weight and we use

⁷ <https://github.com/esheldon/ngmix>

⁸ We use the following definitions of effective source density n_{eff} and the effective shape noise per component σ_{SN} , which are appropriate for the two-point function estimators employed in this work. $n_{\text{eff}} = (\sum_i w_i s_i)^2 / (\Omega \sum_i w_i^2 s_i^2)$ and $\sigma_{\text{SN}}^2 = (\sum_i w_i^2 (e_1^2 + e_2^2)) / (2 \sum_i w_i^2 s_i^2)$ where w_i are the weights, s_i are the sensitivities, e_i are the shear components, Ω is the survey areas and the index i runs over all of the galaxies.

the average sensitivity over both directions, as described in Jarvis et al. (2015)

2.2 Shear Measurement Pipeline 2: im3shape

The IM3SHAPE⁹ pipeline is built on the IM3SHAPE code described in Zuntz et al. (2013), with configuration and modifications for its application to DES SV data described in Jarvis et al. (2015). IM3SHAPE is a forward-modelling maximum likelihood code that uses a Levenberg-Marquardt algorithm to fit (in the configuration used here) two different models to galaxy images, one a de Vaucouleurs bulge and the other an exponential disc, including the effect of the PSF and pixelization. The better-fitting model is then used to give an ellipticity estimate. Maximum-likelihood parameter sets computed by IM3SHAPE and similar codes have a bias we refer to as *noise bias* (Refregier et al. 2012; Kacprzak et al. 2012). This bias is removed using a calibration scheme based on the work of Kacprzak et al. (2012). The scheme is applied to an ensemble of galaxies using the mean bias calibration for the ensemble; different subsets of objects thus use different correction factors. The final IM3SHAPE catalog has an effective number density of $\simeq 4.1$ galaxies per square arcminute. Each source in IM3SHAPE has a weight, two additive noise bias corrections (one each for e_1 and e_2) and a single multiplicative correction.

2.3 Photometric Redshifts

Based on an extensive comparison of four photo- z methods⁹ impacts on the two-point correlation function in Bonnett et al. (2015) and a comparison of a much larger set of photo- z methods in Sánchez et al. (2014), we have selected SkyNet (Bonnett 2015; Graff & Feroz 2013) for our fiducial photo- z tomography. Galaxies are split into tomographic bins of equal lensing weight for the NGMIX catalog according to the mean of the photo- z PDF for each galaxy produced from SkyNet. The resulting tomographic bin boundaries are then used for galaxies in both shear catalogs. For a given shear code, the redshift distribution of each tomographic bin is estimated from summing the redshift probability distributions of each individual galaxy according to their weights assigned by the shear code. The relative agreement between the photo- z estimates and its impact on the correlation function is discussed in more detail in Bonnett et al. (2015).

3 MOCK CATALOGS

We use a set of 126 mock catalogs to compute the covariance matrix of the shear correlation functions, E/B-mode statistics, power spectra and null statistics described in the following sections. These mock catalogs are constructed from seven sets of simulations consisting of three N-body light cones pieced together along the line of sight. We use 1050 $h^{-1}\text{Mpc}$, 2600 $h^{-1}\text{Mpc}$ and 4000 $h^{-1}\text{Mpc}$ boxes with 1400^3 , 2048^3 and 2048^3 particles respectively. We use a flat, ΛCDM model with $\Omega_m = 0.286$, $\Omega_\Lambda = 0.714$, $n_s = 0.96$, $h = 0.7$, $\Omega_b = 0.047$, $w = -1$ and $\sigma_8 = 0.820$. The initial conditions

⁹ <https://bitbucket.org/joezuntz/im3shape>

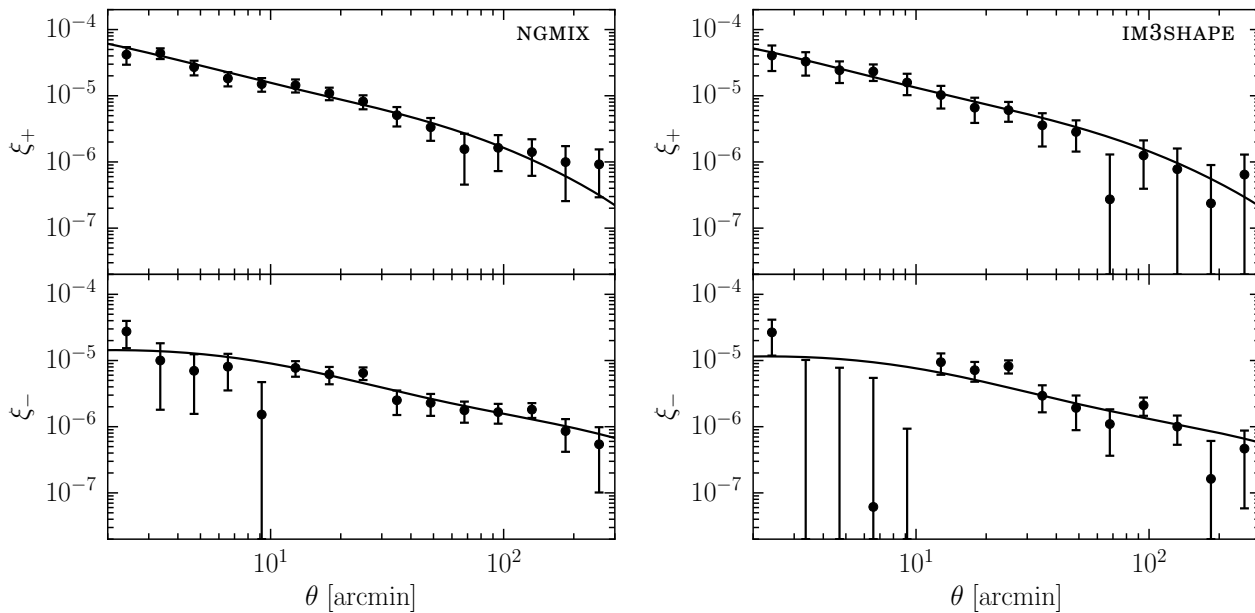


Figure 1. The measured shear correlation functions $\xi_{+/-}$ for a single tomographic bin for the NGMIX shape catalog (left) and IM3SHAPE shape catalog (right). The single tomographic bin corresponds to redshift distribution shown in Figure 3, $z \approx 0.3 - 1.3$. Note that the redshift distributions of the two catalogs are not identical, so that the shear correlation functions are not expected to match. A detailed comparison of the two catalogs is described in Section 6.2. Negative measurements are shown as upper limits. The error bars show the 1σ uncertainties from the mock catalogs with the appropriate level of shape noise for each shear pipeline. The black solid lines show the predictions from a flat, Λ CDM model described in Section 3 — not chosen to fit the data.

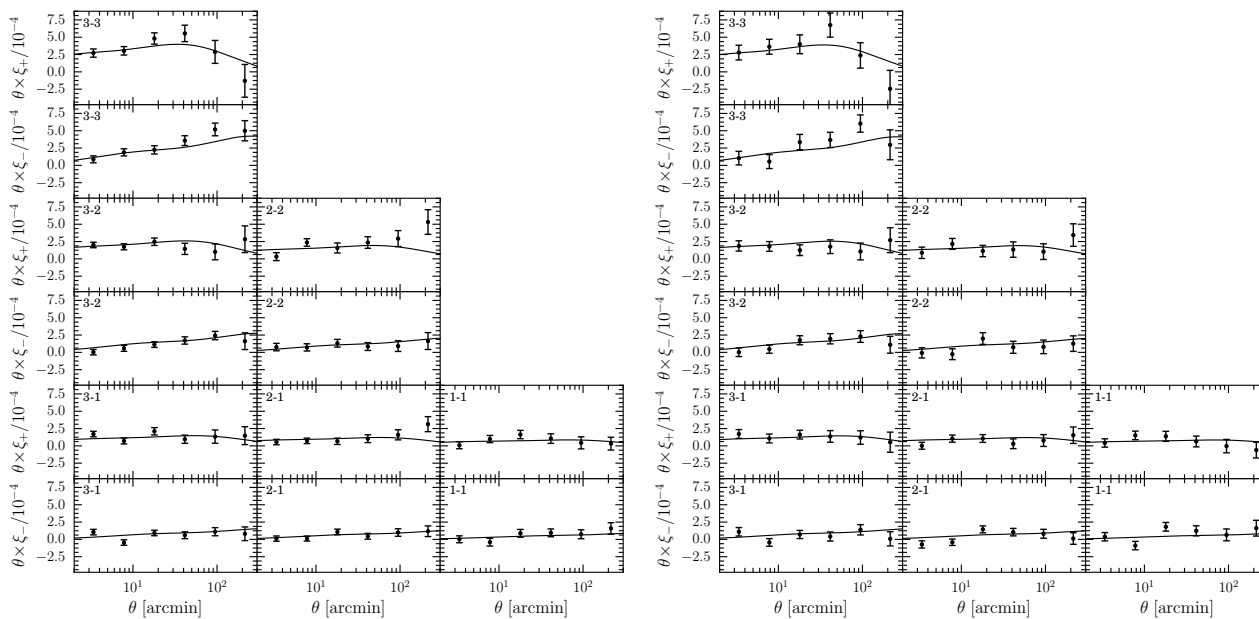


Figure 2. The measured shear correlation functions $\xi_{+/-}$ times θ in six angular bins and three tomographic bins for the NGMIX shape catalog (left) and IM3SHAPE shape catalog (right). The tomographic bins correspond to those shown in Figure 3, $z \approx 0.30 - 0.55, 0.55 - 0.83, 0.83 - 1.30$, and are labeled from 1 to 3, increasing with redshift. Thus, panel ‘3-2’ shows the cross-correlation between the highest and middle redshift bins. The error bars show the 1σ uncertainties from the mock catalogs with the appropriate level of shape noise for each shear pipeline. As in Figure 1, the black solid lines show the predictions from our fiducial Λ CDM model — not chosen to fit the data.

are generated at redshift 49 with `2LPTic`, a second-order Lagrangian perturbation theory initial conditions generator (Croce et al. 2006) using linear power spectra from the `CAMB` Boltzmann code (Lewis & Bridle 2002). The N-body evolution is computed with an efficient dark-matter-only version of the `Gadget-2` code (Springel 2005), `LGadget-2`. We have implemented our own on-the-fly light cone generator directly into the `LGadget-2` code (Busha et al. in preparation). We produce a full-sky light cone which formally replicates the N-body box eight times. However, each final simulation covers only one octant of the full-sky, $\simeq 5,000$ square degrees, eliminating the replications. As the DES SV area with weak lensing measurements is only 139 square degrees, we divide each simulation into 18 different pieces using the observed SV mask to construct 126 total mock catalogs. This procedure has the advantage of properly computing the halo sample variance contributions to the lensing covariance matrices due to the fact that each patch is embedded in the large-scale modes of the box.

We place lensing sources randomly in angle and with the redshift distribution of the tomographic bins defined above. Then the weak lensing shear for each source is computed using the `CALCLENS` ray-tracing code (Becker 2013). In this application of `CALCLENS`, we use the pure spherical harmonic transform version with `Nside=8192`. Appendix B presents tests of the underlying simulations in comparison to simple expectations from fitting functions to the matter power spectrum. We find that the simple expectations from matter power spectrum fitting functions agree with the simulation to within sample variance, but that some resolution issues remain on small scales. Note, however, that these small scales are excluded from the companion cosmological analysis (DES et al. 2015) and that despite the resolution issues, we find excellent agreement between the covariances computed from the mock catalogs and the halo model, as discussed below. Thus for purposes of computing covariance matrices, the mock catalogs we have constructed are sufficient. Future work may require higher-resolution shear fields for covariance estimation.

Finally, we generate the shape noise and other properties in the mock by randomly drawing from the observations separately for each tomographic bin. Importantly, we draw the intrinsic shape of each mock shear source separately from its other properties, like signal-to-noise, size, etc. Properties which have intrinsic spatial dependence in the survey (e.g. seeing, airmass, etc.) are drawn from the nearest real galaxy to each mock galaxy. See Section 6.3 for more details. These procedures randomise the shear field in the data and ensure that the mock catalogs have no correlations between the systematic parameters and the shear field.

4 MEASUREMENTS OF COSMIC SHEAR TWO-POINT STATISTICS

In this work, we focus on cosmic shear measurements made with two-point statistics, which are detailed in the following sections. A companion paper (DES et al. 2015) presents the associated cosmological parameter constraints using these measurements, which use the real-space two-point correlation functions as the fiducial two-point estimator. We sum-

marize results from alternate estimators in Section 4.3 and Appendix A.

4.1 Real-space Two-point Function Estimators

We follow Miller et al. (2013) and estimate the two-point functions with

$$\begin{aligned}\xi_{\pm} &= X_{+} \pm X_{\times} \\ X_{+/\times} &= \frac{\sum_{i,j} w_i w_j (e-c)_{+/\times}^i (e-c)_{+/\times}^j}{\sum_{i,j} w_i w_j s^i s^j}\end{aligned}\quad (1)$$

where i, j index the galaxies in the two sets we are correlating. Here $e_{+/\times}$ are the estimated shears from the lensing analysis projected into the + (tangential) and \times (cross) components rotated into the reference frame connecting each pair of galaxies $\{i, j\}$ in the sum. The w_i are weights applied to each galaxy (typically inverse variance weighting; see Sec. 2 for each lensing code). The s^i are multiplicative noise bias and/or lensing sensitivity corrections that are applied to the shears. We follow Miller et al. (2013) and apply these corrections to the entire population of shears as opposed to applying them to each shear individually. We compared several different methods for incorporating the sensitivities into the two-point function estimator and find that they differ by at most $\sim 2\%$. The c^i are the additive bias corrections used for `IM3SHAPE` and are zero for `NGMIX`. Finally, we use `TreeCorr`¹⁰ (Jarvis et al. 2004) to compute the shear correlation functions.

4.2 Real-space Correlation Functions

The real-space correlation functions without tomography are shown in Figure 1. We show `NGMIX` on the left and `IM3SHAPE` on the right, with ξ_{+} in the top rows and ξ_{-} in the bottom rows. Open points are negative with the error bars reflected about the origin. The redshift distribution of sources for the non-tomographic analysis is shown in the top panel of Figure 3 for the `SkyNet` code.

We generate estimates of the 1σ uncertainties for each measurement by computing the covariance of the two-point functions over the simulation mock catalogs described in Section 3. These mock catalogs are built separately for each shear catalog in order to match the non-tomographic redshift distribution of the sources. The correction factor described in Hartlap et al. (2007) is then applied to produce an unbiased estimate. The significance of the resulting measurement is then calculated from this covariance as

$$S/N = \frac{\boldsymbol{\xi}_{\text{data}} \mathbf{C}^{-1} \boldsymbol{\xi}_{\text{model}}}{\sqrt{\boldsymbol{\xi}_{\text{model}} \mathbf{C}^{-1} \boldsymbol{\xi}_{\text{model}}}}, \quad (2)$$

where \mathbf{C}^{-1} is the inverse covariance matrix estimated from the mock catalogs, $\boldsymbol{\xi}_{\text{data}}$ is the vector of real-space shear two-point function measurements from the data, and $\boldsymbol{\xi}_{\text{model}}$ is the vector of real-space shear two-point function measurements predicted from the cosmological model given above. This quantity corresponds to the signal-to-noise of a least-squares estimate of a scaling parameter comparing our measurements to the theoretical model. This signal-to-noise

¹⁰ <https://github.com/rmjarvis/TreeCorr>

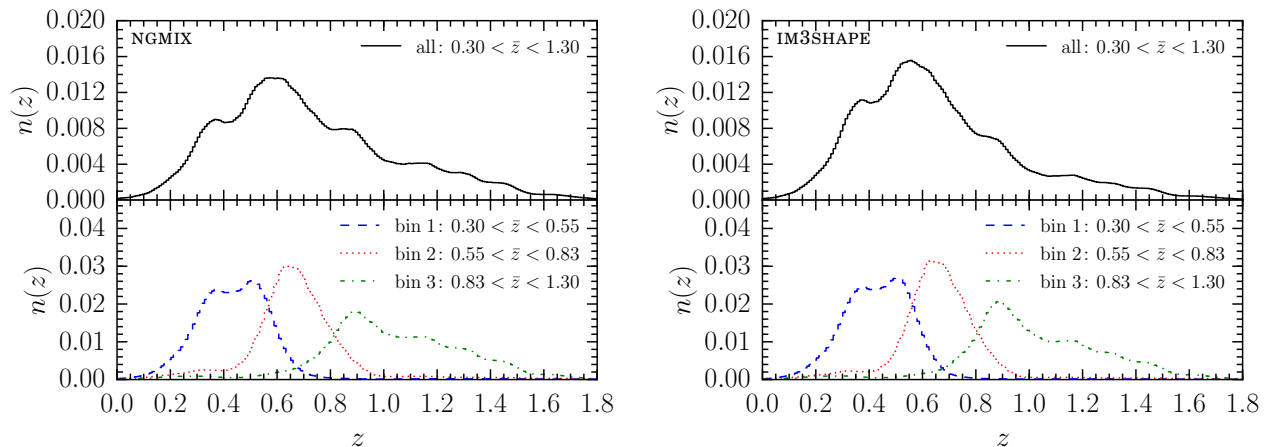


Figure 3. The estimated redshift distributions from *SkyNet* for the NGMIX shape catalog (left) and the IM3SHAPE shape catalog (right). The full $n(z)$ for objects with mean redshifts in the redshift range $0.3 < \bar{z} < 1.30$ (top) and the $n(z)$ for three tomographic bins (bottom) are shown. The redshift distributions are estimated by summing and rescaling the photometric redshift probability distributions for each galaxy in the tomographic bin using the weights applied to the shear catalog.

measure will be an underestimate if the model employed is not well matched to the data. However, given the good match of our fiducial model to the data as shown in Figures 1 and 2, the degree to which the signal-to-noise is underestimated is small in this case. We use the *COSMOSIS* package¹¹ by Zuntz et al. (2014) to compute the shear correlation functions with the Takahashi et al. (2012) non-linear power spectrum fitting function. See the companion paper presenting cosmological constraints from these measurements for additional details (DES et al. 2015). The covariance matrix has been validated through comparisons to both a detailed halo model prediction and jackknife estimates in single mock patches versus the survey data, which are discussed in detail in the Section 5. We find non-tomographic cosmic shear detections at 6.5σ and 4.7σ significance for NGMIX and IM3SHAPE respectively.

Figure 2 shows the full three-bin tomographic shear correlation function measurements for NGMIX on the left and IM3SHAPE on the right. The redshift distributions of the three tomographic bins for the *SkyNet* code are given in the lower panels of Figure 3. In order to compute the covariance matrix of these measurements, we use the same procedure in the mock catalogs as for the non-tomographic case, except that we use the tomographic redshift distributions to assign the mock galaxies to different tomographic bins. We additionally draw the shape noise in the mock from only the galaxies in the data in the same tomographic bin. We find overall tomographic cosmic shear detections of 9.7σ and 7.0σ for NGMIX and IM3SHAPE, respectively. Note that the NGMIX catalog has more sources and extends to slightly higher redshift on average, yielding higher significance detections of cosmic shear.

In Figures 1 and 2, the solid black line shows the expected amplitude and shape of the shear correlation functions in the cosmological model given above. This curve is not a fit, and is merely presented as a reference for com-

parison. Due to the fact that the two catalogs have different redshift distributions, a direct comparison of the shear correlation functions between the two catalogs is not possible without further work matching the two catalogs and accounting for the shared shape noise, sample variance, and image noise between the two catalogs. This matched comparison is described further in Sec. 6.2.

4.3 Alternative Two-point Statistics

In Appendix A, we describe results from two alternative two-point statistics of the shear field. These include the methods of: (i) Becker & Rozo (2014), which use a weighting of the real-space correlation estimates to construct efficient estimates of the C_ℓ values and (ii) a second estimation of the spherical harmonic shear power spectrum using *PolSpice*¹² (Szapudi et al. 2000; Chon et al. 2004). Note that these estimators weight the data at different angular scales differently than the default two-point correlation functions so that we do not expect to get identical results in terms of the significance of the cosmic shear detection. We do find detections of cosmic shear that are consistent with the conventional real-space estimators we use by default, indicating no strong preference for any given estimator. Tests of B-mode statistics from these estimators are discussed in Sec. 6.1, where we again find consistency between different two-point function estimation methods.

5 ESTIMATING AND VALIDATING THE COVARIANCE MATRIX

In this section, we present our covariance matrix and a set of validation tests. The fiducial covariance matrix for our measurements is estimated from the mock catalogs presented in Section 3. First we compare the covariance matrix from

¹¹ <https://bitbucket.org/joezuntz/cosmosis>

¹² <http://www2.iap.fr/users/hivon/software/PolSpice/>

the mock catalogs to halo model computations. Second, we compare jackknife covariances in the data to the jackknife covariance computed from the mock catalogs. This procedure allows us to look for additional sources of noise and correlations in the data that are not present in the mock catalogs.

5.1 Simulation and Halo Model Comparison

We compare the covariance matrix computed from the simulations to that obtained from a halo model in Figure 4. The simulation-based covariance matrix is computed by populating the mock catalogs with shear sources as described above in Section 3, and then computing the covariance of the measurements performed on the full ensemble of mock catalogs. The halo model covariance was computed with the CosmoLike covariance module (see Eifler et al. 2014b and Krause et al. 2015 for details). Further details of our halo model computation and the full tomographic covariance matrix are given in Appendix C. Briefly, we include the Gaussian, non-Gaussian and halo sample variance terms (e.g., Takada & Hu 2013) and compute the halo model covariance at the same cosmology and with the same redshift distribution as was used in the mock catalogs.

We compare the general structure of the mock (upper triangle) and halo model (lower triangle) covariance in the left panel of Figure 4, which shows part of the correlation matrix. Here we have shown a subset of the full set of tomographic bin combinations. The full correlation matrix is shown in Appendix C. The right panel compares the amplitude of the two covariances by plotting the variance. Overall, we find good agreement in both structure and amplitude.

We quantitatively test the agreement using a Fisher matrix computation. We compute the expected error on the degenerate parameter combination $\sigma_8(\Omega_m/0.3)^{0.5}$, where σ_8 is the RMS amplitude of the linear matter power spectrum at redshift zero in a top hat window of $8 h^{-1}\text{Mpc}$ and Ω_m is the matter density in units of the critical density at $z = 0$. This combination of parameters is typically the best constrained by low-redshift cosmic shear data sets like the DES SV data. The exact degeneracy is computed in the companion cosmological constraints paper to this work (DES et al. 2015). We use the standard Fisher matrix formalism for cosmic shear (see, e.g., Albrecht et al. 2009) and the same cosmological model as described above. We vary only the spectral index n_s , σ_8 and Ω_m in the Fisher matrix.

We find that the error bars on $\sigma_8(\Omega_m/0.3)^{0.5}$ from the halo model and mock covariances agree to approximately 10% without tomography, with the halo model yielding larger parameter uncertainties. When repeating the same exercise with tomography, we find a larger, $\approx 35\%$ disagreement in the error bars, with the mocks yielding larger errors. However, we expect fluctuations in the uncertainties in parameters computed with the simulations due to the finite number of realizations used for the covariance computation. Dodelson & Schneider (2013) estimate that this effect, in the Gaussian limit, increases the variance in the parameter estimates by a factor of

$$\alpha = 1 + \frac{(N_d - N_p)(N_s - N_d - 2)}{(N_s - N_b - 1)(N_s - N_b - 4)}$$

where N_d is the number of data points, N_s is the number

of simulations and N_p is the number of parameters. This factor is $\approx 1 + N_d/N_s$ in the limit that $N_s \gg N_d \gg N_p$. Thus we expect a fractional uncertainty in the parameter uncertainties of $\approx \sqrt{\alpha - 1}$. In our case with tomography, $N_d = 72$, $N_s = 126$ and $N_p = 1$. With these numbers, we get that the fractional uncertainty in the parameter uncertainty is $\approx 118\%$. Thus the disagreement of $\approx 35\%$ we find with the halo model with tomography is not statistically significant. Without tomography, we find a fractional uncertainty in the uncertainty of $\approx 56\%$, again indicating consistency.

Importantly, these numbers are the fractional uncertainty in the uncertainty. For parameter estimates, the fractional increase in the uncertainty on the parameter, equal to $\sqrt{\alpha}$, is the relevant quantity. For tomography, this fractional increase is $\approx 55\%$ and without tomography it is $\approx 15\%$. Furthermore, we have assumed that the tomographic analysis uses all 72 data points. As described in DES et al. (2015), only 36 of the 72 data points are used for tomography, bringing the fractional increase in the error due to the finite number of realizations down to only $\approx 18\%$. Similar cuts are made for the non-tomographic analysis, using only 16 of the 30 data points. This number of data points results in a fractional increase of the parameter uncertainties of only $\approx 7\%$ for the non-tomographic analysis.

5.2 Jackknife Comparisons to Data

While our mock catalogs include both sample variance and shape noise contributions, any spatially varying systematic effects, like errors in the shear calibration, should be included in the noise model as well. These effects would appear as additional covariance in the shear correlation function measurements beyond the sample variance and shape noise contributions. To search for these potential effects, we use an empirical estimate of the shear correlation function covariance matrix as a statistic to be compared between the data and the mock catalogs. We chose to use the jackknife covariance matrix of the shear correlation functions for the empirical estimate. Any additional sources of noise in the data, which are captured by the spatial scale of our jackknife regions, will show up as a difference between the jackknife covariance as computed in the data versus the mock catalogs.

We estimate the jackknife covariances from the data and our mock catalogs as follows. We divide both the mock catalog and data into 100 spatial sub-regions, employing the k-means algorithm.¹³ These regions are then used to perform jackknife resampling. For the details of jackknife covariance estimation for cosmic shear correlation functions, we refer the reader to a (technical) companion paper where these choices are examined in further detail (Friedrich et al., in preparation, see also Norberg et al. 2009 for an application to galaxy clustering). We use the standard jackknife scheme, where all of the shear sources in an entire subregion are removed for each jackknife resampling, which is called the *galaxy-jackknife* in Friedrich et al. (in preparation).

Note that we are not comparing jackknife covariances with the true covariances, but rather simply the co-variance

¹³ Implemented for python by Erin Sheldon, www.github.com/esheldon/kmeans_radec.

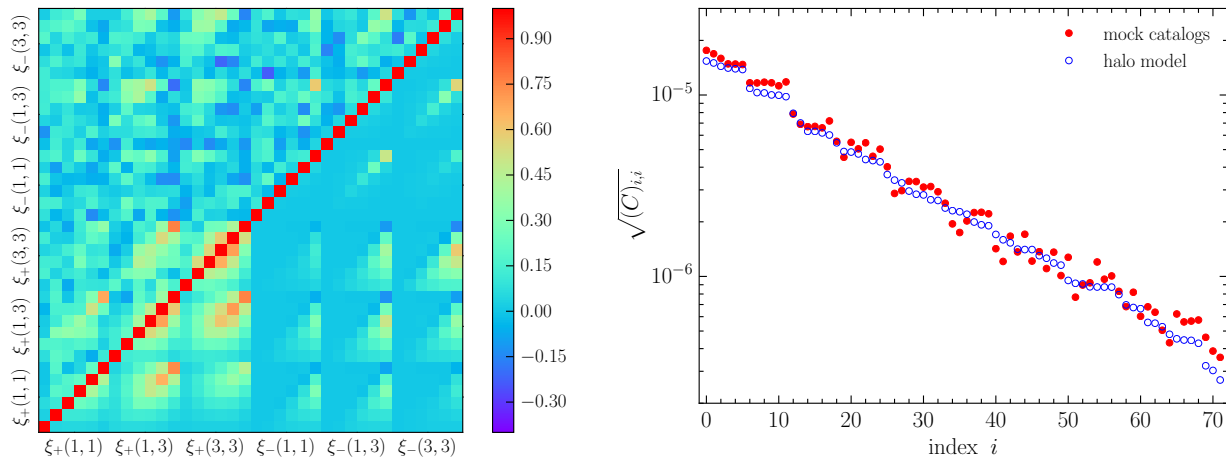


Figure 4. Comparison of the tomographic shear correlation function correlation matrix estimated from the mock catalogs and calculated from the halo model. The left plot shows the correlation matrix from the mock catalogs (upper left) and halo model (lower right). We show only the components for the first and last tomographic bins, plus their cross correlations. On the right, we show the square root of the diagonal elements of both covariance matrices, sorted in reverse numerical order. The open symbols show the results from the halo model and the closed symbols show the results from the mock catalogs.

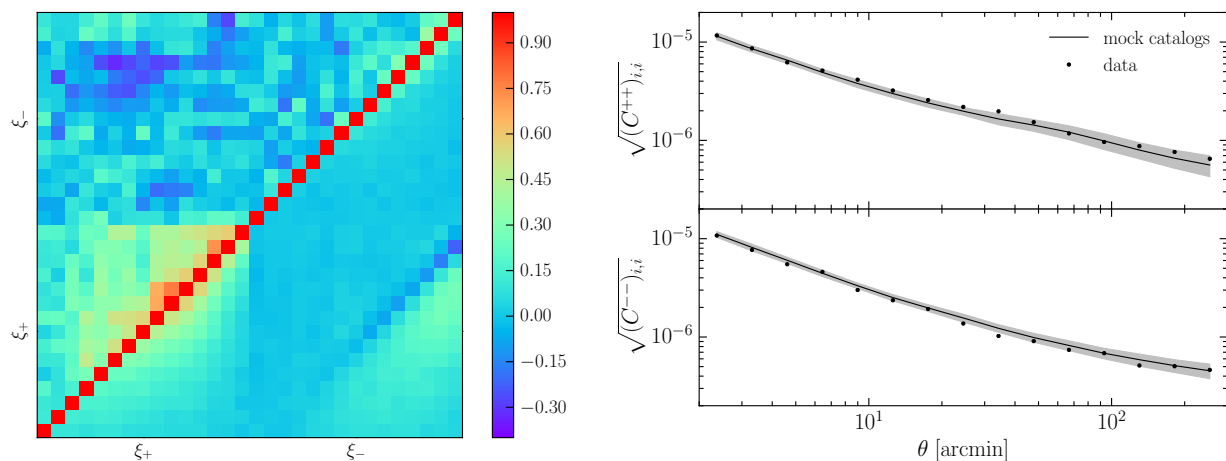


Figure 5. Jackknife covariances in the mock catalogs and the data for the non-tomographic shear correlation functions. The left panel shows the correlation matrix using jackknives in the data for NGMIX (top left) and when averaging the jackknife covariances in the 126 mock catalogues (bottom right). The bottom left quadrant contains the ξ_+ correlations, the top right the ξ_- correlations and the off diagonal components contain the cross-correlations. For each submatrix of the full correlation matrix, the angular scale increases from 2 arcminutes to 300 arcminutes. On the right, we show the diagonal elements of the jackknife covariance matrix in the data for NGMIX (points) and when averaged over 126 mock catalogues (line). The grey band shows the standard deviation of diagonal elements over the 126 mock catalogs.

in the shear correlation function across the DES SV survey to the same statistic computed with the mock catalogs. Thus the absolute correctness of the jackknife covariance matrix is not an issue for our test, since it is just a statistic that is sensitive to the effects for which we wish to search. The performance of empirical covariance measures for cosmic shear surveys is explored in Friedrich et al. (in preparation).

The comparison of our jackknife procedure between the mocks and the data is shown in Figure 5. Here we plot the correlation matrix of the averaged jackknife covariance from the 126 mock NGMIX catalogues (left panel, on the bottom right) and the same computation in the DES SV data (on the top left). The right panel compares the diagonal elements of the jackknife covariance for ξ_+ and ξ_- when av-

eraged over 126 mock catalogs and when computed from the data for NGMIX. Using the Fisher matrix procedure described above, we find that the mean error on $\sigma_8(\Omega_m/0.3)^{0.5}$ from the data jackknife covariance matrix agrees with the mean of the ensemble of errors on this parameter from the mock jackknife covariances to within one standard deviation of the error over the ensemble. Thus we conclude that there are no statistically significant sources of additional variance in the data compared to the mock catalogs.

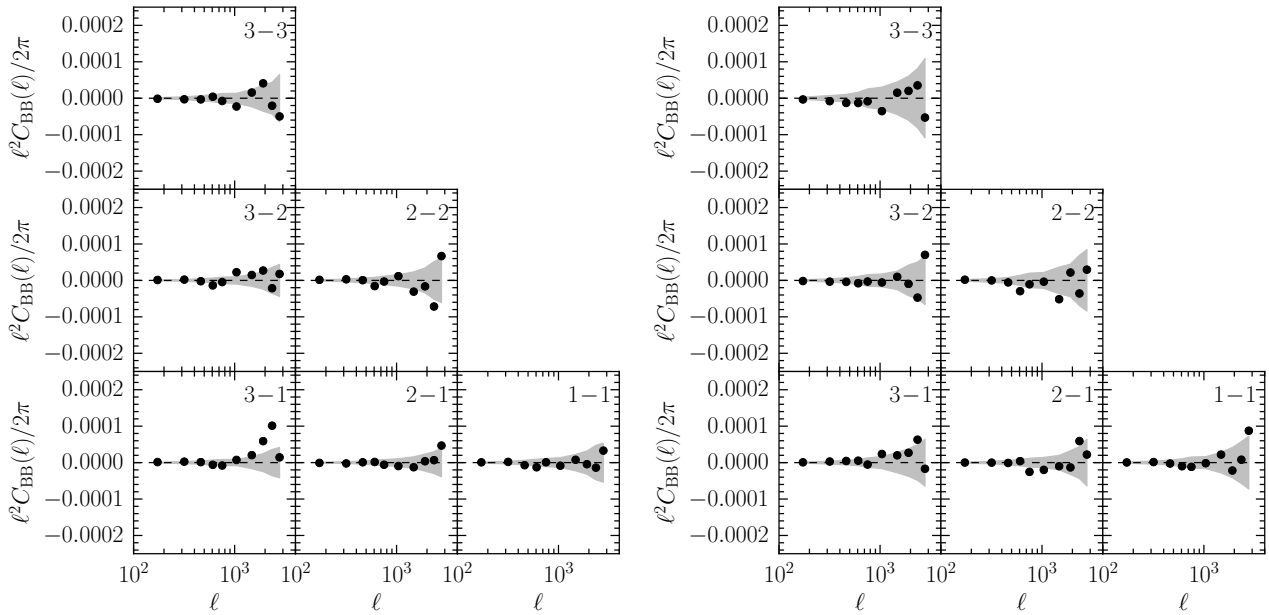


Figure 6. Tomographic B-modes in DES SV data for NGMIX (left) and IM3SHAPE (right). The error bars are calculated from the simulation realizations using the shape noise appropriate for each catalog. The tomographic bins correspond to those shown in Fig. 3 and are labeled from 1 to 3, increasing with redshift. Thus, panel '3-2' shows the cross-correlation between the highest and middle redshift bins. The total $\chi^2/\text{d.o.f.}$, accounting for the correlations between the points in each panel, for NGMIX is 62.5/60 and for IM3SHAPE is 41.2/60.

6 TESTS FOR RESIDUAL SYSTEMATIC ERRORS IN THE COSMIC SHEAR SIGNAL

Systematic errors in shear measurements can be from a wide array of sources ranging from telescope optics and observing conditions to details in the modeling, measurement, and calibration of shapes. The development of tests to identify potential systematic errors is critical to verifying accurate measurement of cosmic shear. Toward this end, we devise a set of tests that should produce a null result when applied to true gravitational shear. The measurement of a significant non-zero result is then an indication of unresolved systematic errors in the shear catalog that could bias measurements.

The DES SV shear catalogs have passed a rigorous set of both traditional and novel null tests that lay the groundwork for validating the precise measurements that will be made with ongoing DES measurements during the main survey observing period. These tests are performed both at the catalog level and during the process of validating specific measurements based on the shear catalogs. We describe the methodology and results of both traditional and new null tests for sources of potential systematic errors in both the non-tomographic and tomographic measured cosmic shear signal in the next two sections.

Catalog-level tests were performed by Jarvis et al. (2015, cf. their Section 8) and included tests for additive systematic errors related to spatial position, the PSF, and galaxy properties. No significant additive systematic errors were found, and they put upper limits on the potential additive systematic contribution to ξ_+ in their Section 8.7. In addition, the overall multiplicative bias of the shear estimates was tested with simulations. They conclude that both catalogs are consistent with having small overall mul-

tiplicative bias, but due to uncertainties in their ability to constrain this value, they suggest marginalizing over a prior on the multiplicative bias with a standard deviation of 0.05. This multiplicative systematic is treated in the cosmological analysis of this data (DES et al. 2015).

6.1 B-mode Measurements

The cosmic shear field can be characterized by E- and B-modes which differ in parity. At first-order in the gravitational potential in General Relativity, cosmic shear produces a pure E-mode field (see, e.g., Bartelmann 2010). However, contaminating signals, like that from the telescope point-spread function, tend to contain both E- and B-modes. Thus one of the first suggested tests of cosmic shear detections was verifying that the B-mode signal is consistent with zero (Kaiser 1992).¹⁴ Many methods have been suggested for B-mode estimation (e.g., Schneider et al. 1998; Seljak 1998; Hu & White 2001; Crittenden et al. 2002; Schneider & Kilbinger 2007; Schneider et al. 2010). Here we use the estimators from Becker & Rozo (2014), which estimate band-powers using linear combinations of the shear two-point functions that optimally separate E- and B-modes (Becker 2013). These estimators are

$$E = \frac{1}{2} \left[\sum f_{+i}\xi_{+i} + \sum f_{-i}\xi_{-i} \right] \quad (3)$$

$$B = \frac{1}{2} \left[\sum f_{+i}\xi_{+i} - \sum f_{-i}\xi_{-i} \right], \quad (4)$$

¹⁴ Small levels of B-modes are produced at second order in the gravitational potential, but these are small enough not to spoil the null test (see, e.g., Hilbert et al. 2009; Krause & Hirata 2010).

where the sums run over the angular bins of the shear two-point functions. The weight vectors $f_{+/-}$ are chosen to simultaneously minimize E- to B-mode mixing while also producing compact band-power estimates in Fourier space. See Appendix A for more details.

In Figure 6, we show a measurement of the tomographic B-mode signal using the Becker & Rozo (2014) band-powers. We find no statistically significant B-mode contamination, with a total $\chi^2/\text{d.o.f.}$ for NGMIX of 62.5/60 and for IM3SHAPE of 41.2/60. The error bars in this case are computed using the mock catalogs above. In Appendix A, we verify this conclusion by computing a complementary measurement of the non-tomographic B-mode signal using an alternate estimation of the spherical harmonic shear power spectrum. We find the B-modes from this alternate technique are consistent with zero with a $\chi^2/\text{d.o.f.} = 4.5/7$ for NGMIX and 6.3/7 for IM3SHAPE. Finally, note that Becker & Rozo (2014) band-power measurements of the non-tomographic B-mode signal are presented in Jarvis et al. (2015) using the methods and mock catalogs of this work. The non-tomographic B-mode measurements were again found to be consistent with zero, with $\chi^2/\text{d.o.f.} = 22.3/20$ for NGMIX and 16.1/20 for IM3SHAPE.

6.2 Consistency Between the Shear Pipelines

We further test for consistency between the shear catalogs split into tomographic bins by selecting only sources which pass the selection cuts for both codes. For this subset of sources, we then compare the shear auto- and cross-correlation functions for each bin. Due to the fact that the two catalogs have the same sample variance, have similar shape noise and have correlated shear measurement errors, the error bars on the difference between the two correlation functions is much smaller than that on the correlation functions themselves. We account for this effect by constructing mock catalogs where a given mock galaxy is assigned its shape noise for each shear measurement code, NGMIX or IM3SHAPE, from the same real galaxy.

This comparison is shown in Figure 7 for the shear correlation function for IM3SHAPE minus NGMIX.¹⁵ We find that the shear correlation functions from the codes are statistically consistent over the full range of scales from 2 to 300 arcminutes, giving a $\chi^2/\text{d.o.f.} = 46.8/72$. Finally, note that this test is similar the differenced shear correlation function test presented in Section 8.6 of Jarvis et al. (2015). For their test, they examine the shear correlation function of the the difference in the NGMIX and IM3SHAPE shear estimates using the matched catalogs. They find that below ≈ 3 arcminutes, the catalogs do not meet the requirements for additive systematic errors, set by the expected precision of the cosmological constraints. The test presented in this work is generally less sensitive, but complementary, to the differenced shear correlation function.

¹⁵ We have completed this test for the ratio of the shear correlation functions and without tomography, finding similar results.

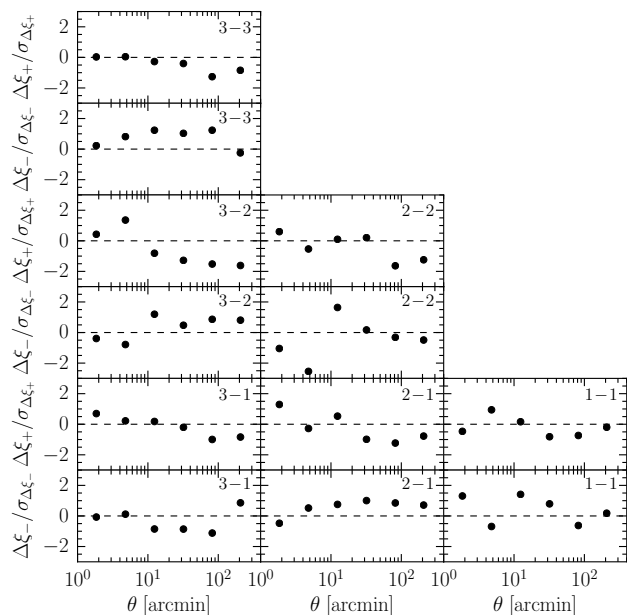


Figure 7. Difference over error in the tomographic correlation functions for matched shear catalogues from NGMIX and IM3SHAPE. We show IM3SHAPE minus NGMIX. The total $\chi^2/\text{d.o.f.}$ accounting for all correlations is 46.8/72.

6.3 Two-Point Null Tests

Even with a carefully chosen set of null tests at the catalog level, it is still possible that systematic errors, which can be due to complex interplays between different aspects of data and analysis, may influence the cosmic shear measurement. To test for any uncorrected systematic errors remaining in the measured cosmic shear signal, we attempt to measure the variation in ξ_+ as a function of survey and galaxy properties that may be correlated with sources systematic errors. For each survey or galaxy property, the shear data is split in half, and the correlation functions of each half are compared. We use a reweighting method to ensure that the redshift distribution of each half is the same in order to remove any cosmological dependence from this null test. If the photo- z s and shear measurements are correct, then the shear correlation functions of the two halves should be consistent to within the noise of the shear measurements and the redshift reweighting. If they are not, this would indicate either uncorrected systematics, selection effects from the split, or non-shear differences in the two halves such as intrinsic alignments.

Due to the fact that each half is drawn from the same area in many cases, the standard error bars computed for the shear correlation functions are not correct for this test. We instead use the mock catalogs described above to compute the error on the difference between the two halves relative to the full sample, accounting for shared sample variance, as described below. It is important to note that this is a simultaneous test of both the photometric redshifts and the shear calibrations. This feature is in fact desirable because both of these quantities can contribute to biases in the shear correlation functions. We have used both the survey property maps described by Leistedt et al. (2015) and also prop-

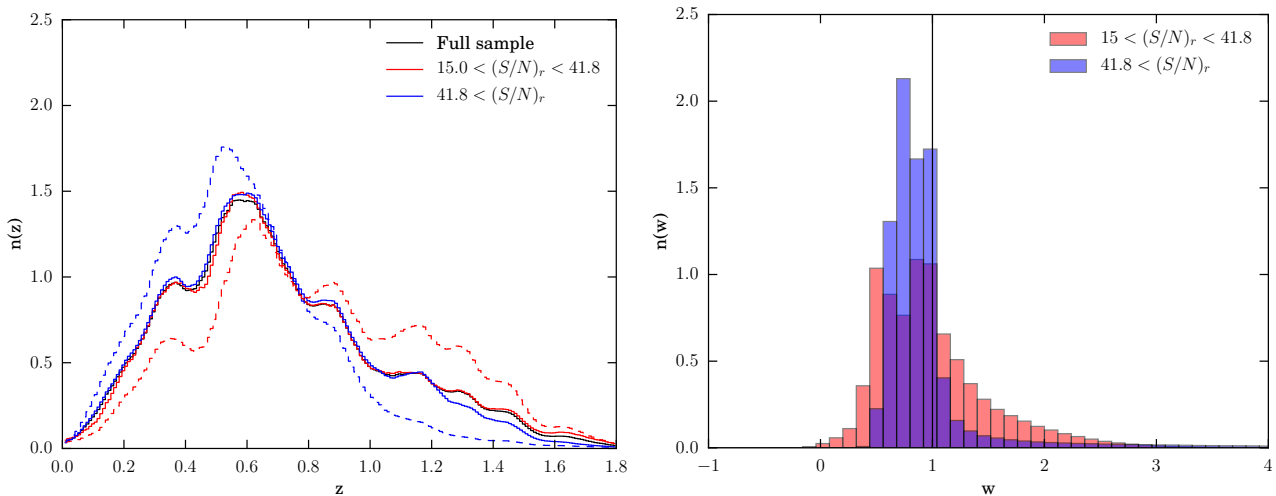


Figure 8. An example of the redshift re-weighting procedure used when comparing the correlation function between galaxies split into bins of galaxy or survey properties. Left: The SKYNET redshift distribution for each half of the NGMIX data, split into upper (blue) and lower (red) bins of signal-to-noise ratio $(S/N)_r$ before (dashed) and after (solid) re-weighting, compared to the full sample $n(z)$ (black solid curve). Right: The distribution of weights applied to each galaxy to produce the solid $n(z)$ lines, generated as described in Sec. 4.5.

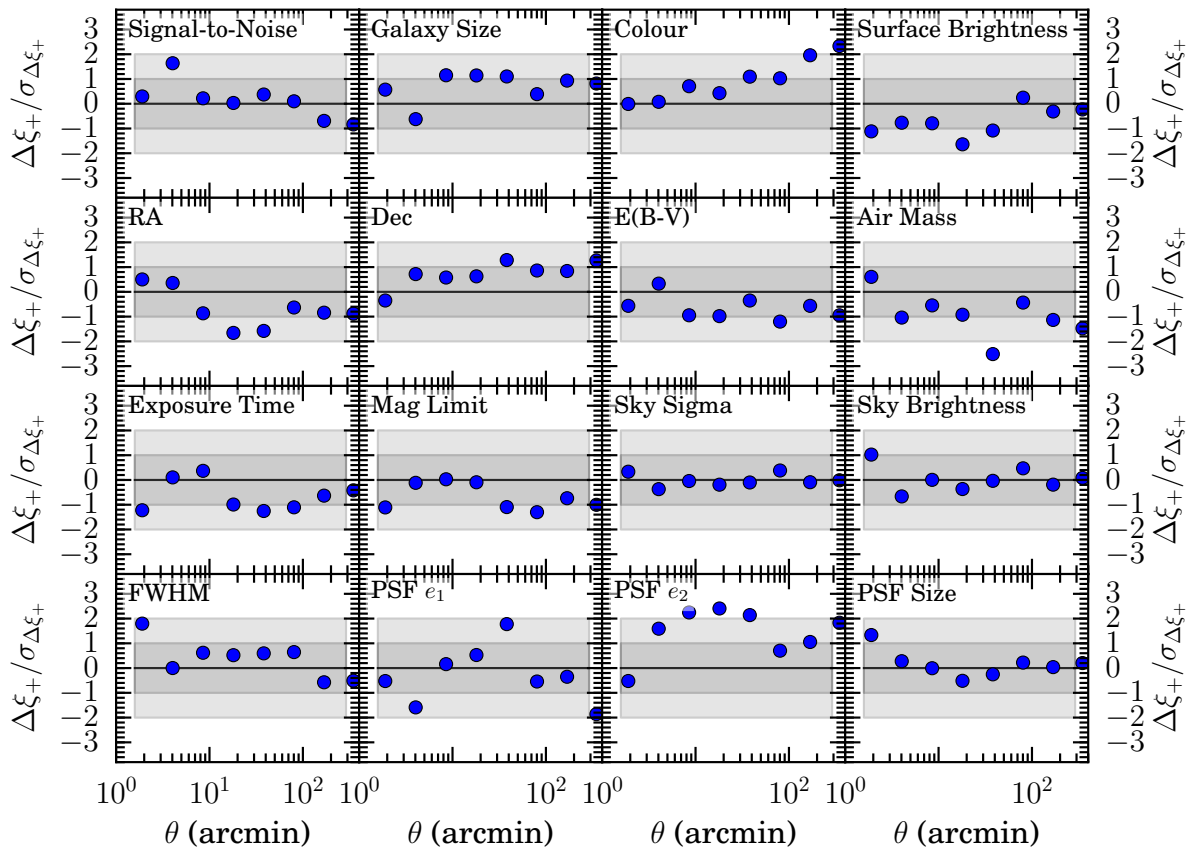


Figure 9. Null tests for the NGMIX two point correlation function based on a variety of catalog and survey properties as described in Table 1. Each panel for a given property shows the difference between the ξ_+ relative to its error for the galaxies in the upper and lower halves of the sample split into bins by the magnitude of the quantity. The two halves of the sample have been reweighted to have the same redshift distribution. The error on the difference is computed directly via the mock catalogs. Grey bands are shown representing the 1σ and 2σ variance at each value of θ . Adjacent points in angle are correlated.

erties directly produced by the shape measurement codes. The 16 various systematic parameters are described in Table 1. Finally, Jarvis et al. (2015) found that making cuts on signal-to-noise and size could lead to a selection bias in the population of shear values due to preferentially selecting galaxies that look more or less like the PSF. We attempt to minimize this problem by using the “round” measures of signal-to-noise, size and surface brightness.

6.3.1 Methodology

The galaxies in each half-sample must be reweighted so that the total $n(z)$, computed from summing the individual $p(z)$ for each galaxy according to its weight, matches between the two half-samples. Matching the redshift distributions of the two halves removes any cosmological dependence in each null test. For the data, the extra weights are computed using Ridge Regression (or Tikhonov regularization) (Pedregosa et al. 2011). We use the Ridge Regression algorithm to solve for an additional weight for each galaxy, which when used with the shear measurement weights described in Section 2 to compute the $n(z)$, produces a matching redshift distribution between the two half-samples. The Ridge Regression algorithm solves the linear least-squares problem with an additional regularization parameter α , minimizing

$$\|\mathbf{R}\mathbf{v} - \mathbf{t}\| + \|\alpha(\mathbf{v} - \mathbf{I})\| \quad (5)$$

where $\|\dots\|$ denotes the least-squares norm, \mathbf{R} is the matrix of galaxy $p(z)$'s each weighted by the lensing weights given in Section 2,

$$\mathbf{R} = \begin{bmatrix} w_1 p_{11} & w_2 p_{12} & w_3 p_{13} & \dots & w_n p_{1n} \\ w_1 p_{21} & w_2 p_{22} & w_3 p_{23} & \dots & w_n p_{2n} \\ w_1 p_{31} & w_2 p_{32} & w_3 p_{33} & \dots & w_n p_{3n} \\ \dots & \dots & \dots & \dots & \dots \\ w_1 p_{m1} & w_2 p_{m2} & w_3 p_{m3} & \dots & w_n p_{mn} \end{bmatrix} \quad (6)$$

for n galaxies and m photo- z bins with lensing weights w_i and galaxy $p(z)$'s p_{ji} , \mathbf{t} is the target photo- z distribution, \mathbf{v} is the vector of new weights for which we are solving and \mathbf{I} is the identity vector. The parameter α governs the flexibility of the weight selection – the smaller the value, the better matched the reweighted $n(z)$ are — and is adjusted to prevent a significant contribution of negative or large weight values, which may impact the validity of the null tests. We find that $\alpha = 5 \times 10^{-11}$ produces an optimal match between the two half-samples while keeping the weights \mathbf{v} sufficiently regular for our photo- z s and lensing weights. This value may not generalize to other lensing weights or photo- z s. We match the redshift distribution of each half-sample to that of the full sample (i.e. \mathbf{t} is the redshift distribution of the full sample). This procedure is more stable than matching one half to another since smaller weights are needed for each half. The application of the Ridge Regression algorithm then produces a new weight \mathbf{v} , which is combined multiplicatively with the lensing weight in the calculation of the correlation functions. The resulting reweighting for galaxies split into bins of low and high galaxy detection signal-to-noise for NGMIX is shown in Fig. 8. The left panel shows the $n(z)$ for each half before (dashed) and after (solid) reweighting compared to the full sample. The corresponding weight histograms are shown in the right panel.

We use the 126 DES SV-shaped mock catalogs described above to compute the variance and significance of the differences between the shear correlation functions in each half-sample. In the mock catalogs, we select a subset of galaxies in narrow redshift slices to match the $n(z)$ distribution for the full galaxy catalog. Random shape noise is generated from the shear catalog and applied to the mock catalogs, and the property with which we split the galaxy sample in half is then mapped onto the galaxies in each mock via a nearest neighbour algorithm in angular position, and redshift. This preserves the same spatial patterns as exist in the data, but the shears have been randomised so that there is no correlation with this property. We then apply the same procedure to each mock as applied to the data to directly compute the error bars on the difference via Monte Carlo, with the exception of using the true mock point redshift values to reweight the $n(z)$ histograms of each half instead of a $p(z)$ estimate for each galaxy. We expect this difference will only underestimate the variance. Any statistically significant deviations then indicate that there may be a residual systematic error in the shear catalogs related to the quantity split upon, which has affected the measured two-point correlation function.

6.3.2 Results

The split null tests on ξ_+ are presented in Figure 9 for NGMIX and Figure 10 for IM3SHAPE. This is repeated in Appendix D for ξ_- . For each quantity (panel), the difference in ξ_+ is shown at each value of θ relative to the 1σ error in the difference from the mock catalogs. Grey bands corresponding to 1σ and 2σ errors are shown for comparison. The corresponding statistical significance of the null tests for IM3SHAPE and NGMIX are given in Table 1. We find that for both NGMIX and IM3SHAPE the null tests pass with deviations smaller than 2σ ($\chi^2/\text{d.o.f.} = 17.8/8$) for all tests except for NGMIX airmass. Note that because NGMIX has a higher source density, it is generally more sensitive to residual systematic errors in these tests. While this detection is still weak, it warrants evaluating whether this difference in the galaxy population halves will have a significant bias on the correlation function. To test this, we also show in Table 1 the difference $\Delta\xi_+ = \xi_{+(\text{upper})} - \xi_{+(\text{lower})}$ relative to the 1σ error on the full sample measurement. For NGMIX airmass, this difference is approximately one-third of the statistical error on the measurements and consistent with the level of bias in several other quantities. Of slightly lesser significance are splits in the magnitude of NGMIX PSF e_1 and e_2 , for which PSF e_2 has the largest difference in ξ_+ between upper and lower halves — though still small compared to the statistical error.

There is some subtlety in interpreting the significance of these null tests. First, due to physical effects not accounted for in the simulations, some tests could yield non-zero results but not indicate systematic errors in the data analysis itself. For example, if the level of intrinsic alignments differs between galaxies split by colour, then these null tests could fail and yet the shear measurements themselves could be free of systematic errors. Second, these tests could also, in principle, flag differences between the shear calibrations of galaxies of different types, which although interesting, may not ultimately impact cosmological constraints from

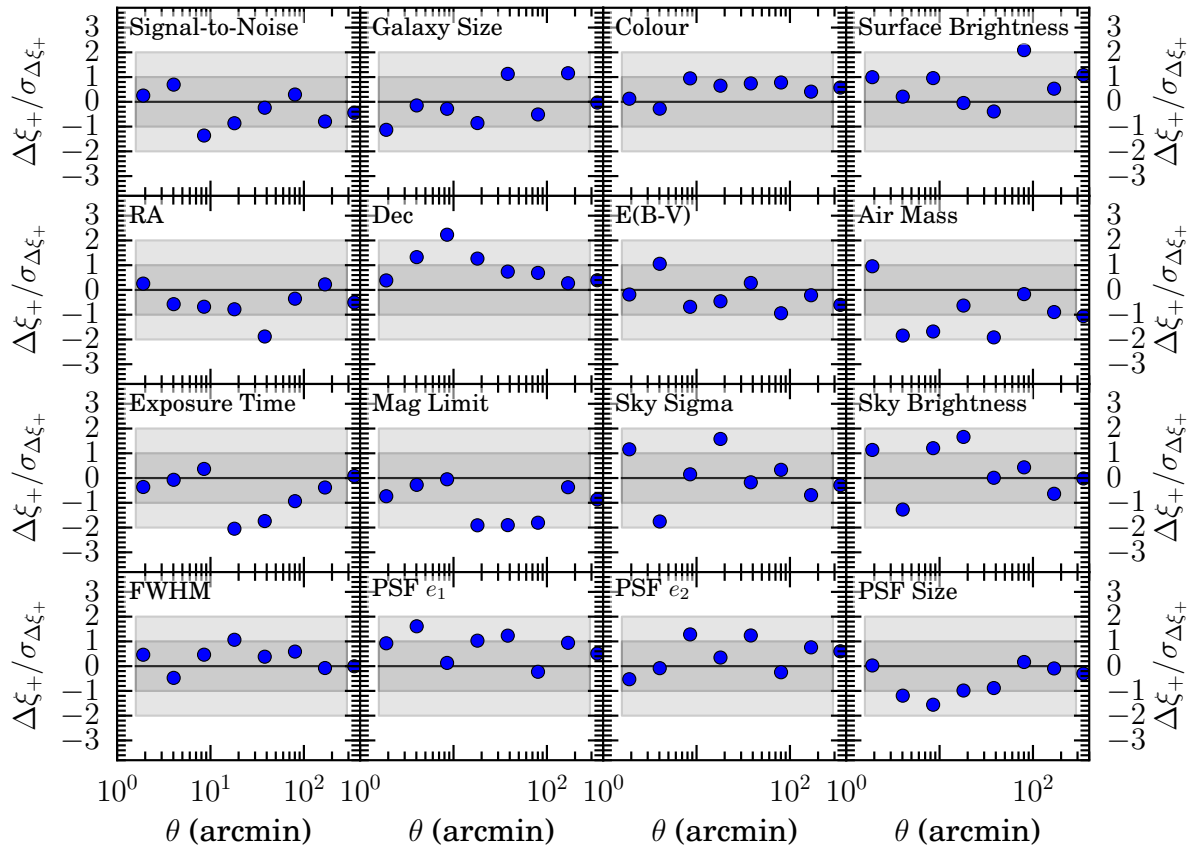


Figure 10. Null tests for the IM3SHAPE two point correlation function based on a variety of catalog and survey properties as described in Table 1. See Fig. 9 for details.

Property	χ^2 [d.o.f. = 8]	$\Delta\xi_+/\sigma(\xi_+)$	Description
	NGMIX (IM3SHAPE)	NGMIX (IM3SHAPE)	
Signal-to-Noise	4.9 (5.2)	0.05 (0.49)	Signal-to-noise of galaxy detection
Galaxy Size	5.3 (10.7)	-0.3 (0.15)	Galaxy size (deconvolved with PSF)
Galaxy Colour	7.3 (2.2)	-0.31 (-0.32)	$g - z$ colour
Surface Brightness	7.8 (8.7)	0.33 (-0.32)	Galaxy surface brightness
RA	7.0 (8.8)	0.24 (0.28)	Galaxy right ascension
Dec	4.0 (6.2)	-0.24 (-0.57)	Galaxy declination
E(B-V)	5.1 (6.2)	0.23 (0.06)	Mean extinction
Air Mass	20.7 (13.8)	0.31 (0.46)	Mean r -band air mass
Exposure Time	4.7 (6.8)	0.18 (0.3)	Mean total r -band exposure time
Mag. Limit	4.4 (7.4)	0.18 (0.45)	Mean r -band limiting magnitude
Sky Sigma	1.7 (13.0)	-0.02 (-0.08)	Mean r -band RMS sky brightness
Sky Brightness	5.0 (14.3)	-0.05 (-0.27)	Mean r -band sky brightness
FWHM	6.4 (3.3)	-0.23 (-0.13)	Mean r -band PSF FWHM
PSF e_1	16.8 (13.5)	0.12 (-0.37)	Galaxy PSF e_1
PSF e_2	17.1 (7.5)	-0.58 (-0.22)	Galaxy PSF e_2
PSF Size	2.6 (5.6)	-0.1 (0.42)	Galaxy PSF size

Table 1. Summary of null tests for NGMIX and IM3SHAPE. Results are given as NGMIX (IM3SHAPE). The χ^2 values are given for the differences between the two-point correlation function calculated from galaxies that fall within one of two bins in each catalog or survey property. Also shown is the magnitude of the difference relative to the 1σ error of the measurement of ξ_+ on the full sample.

the full sample, which could be unbiased on average. Third, as stated above, it is not clear from these tests alone if any deviations are due to the shear measurements or the photometric redshifts. Finally, note that the χ^2 values from these tests are not independent, due to correlations in the underlying quantities used to construct the tests (e.g., the survey depth is correlated with the seeing). We have performed a large number of null tests, so to the extent that the χ^2 values between many of the tests should be independent, we do expect some apparent deviations purely from statistical fluctuations. However, we have not attempted to combine the tests in order to quote an overall significance.

7 CONCLUSIONS

In this work, we present cosmic shear two-point measurements from Dark Energy Survey Science Verification data. We find an overall detection significance of 9.7σ for our higher source density catalog, NGMIX. We additionally present multiple advances in band-power estimation, covariance estimation, simulations versus theory, and null tests for shear two-point correlations. Through this work we demonstrate that our measurements are robust and free of statistically significant systematic errors.

We demonstrate that the covariance matrices derived from the DES SV mock simulations presented in this work are consistent with the halo model, including the halo sample variance terms. We also compare the variance in the mock catalogs to the variance in the DES SV data by comparing jackknife covariances computed in the data and mock catalogs. The structure of the covariance matrices is very similar and we detect no statistically significant sources of additional variance in the data.

We find that the B-mode signals in the data are consistent with zero and that the two shear estimation codes agree well. We additionally present a set of simultaneous null tests of the photo- z s and shear measurements, performed by splitting the shear sample in half according to some parameter and comparing the shear correlation functions of the halves. We find that these tests pass with no statistically significant indications of biases. We expect null tests similar to those developed here to have increased utility in future cosmic shear analyses, where the statistical power is larger and the requirements for controlling systematic errors and shear selection effects are more stringent. The DES itself will have nearly $\approx 36\times$ more data and will measure cosmic shear at significantly higher signal-to-noise, so that these tests will be very useful.

Future cosmic shear two-point function measurements in the Dark Energy Survey face a variety of challenges. First, while we have a sufficient number of simulations for the SV data, simulating the increased area of the full DES will present a significant computational challenge. This challenge will need to be met by a combination of large simulation campaigns, information compression schemes applied directly to the data, and combinations of theoretical models for the covariances with simulations in order to reduce the noise in the covariance matrix elements. Second, in order to use simulations to evaluate the statistical significance of null tests on future DES data, like those presented in this work, we will need to increase the fidelity of the treatment of both

the galaxies and the shear signals. Third, we must better address the formal aspects of the construction of the two-point function statistic estimators in order to make higher precision measurements. Finally, while this work has focused exclusively on broad-bin tomography of the two-point function measurements of cosmic shear, future exploration of higher order correlation functions and finer tomographic binning will be needed to extract the full amount of cosmological information from cosmic shear data. Fortunately, none of these issues are fundamentally intractable and we expect that the new techniques presented in this work will be of great assistance in making future cosmic shear measurements with DES data.

ACKNOWLEDGEMENTS

We are grateful for the extraordinary contributions of our CTIO colleagues and the DECam Construction, Commissioning and Science Verification teams in achieving the excellent instrument and telescope conditions that have made this work possible. The success of this project also relies critically on the expertise and dedication of the DES Data Management group.

MRB is grateful for the support of the University of Chicago Research Computing Center, and especially Doug Rudd, for the time used to carry out the N-body simulations carried out in this work. MRB would also like to thank Stewart Marshall for his ongoing assistance in using SLAC computing resources. This work used the Extreme Science and Engineering Discovery Environment (XSEDE), which is supported by National Science Foundation grant number ACI-1053575. JAZ, MAT, SLB acknowledge support from the European Research Council in the form of a Starting Grant with number 240672. MRB and RHW received partial support from NSF-AST-1211838 and from a DOE SciDAC grant. DG was supported by SFB-Transregio 33 'The Dark Universe' by the Deutsche Forschungsgemeinschaft (DFG) and the DFG cluster of excellence 'Origin and Structure of the Universe'. AA, AR, AN are supported in part by grants 20021_14944 and 20021_1439606 from the Swiss National Foundation. Jarvis has been supported on this project by NSF grants AST-0812790 and AST-1138729. Jarvis, Bernstein, and Jain are partially supported by DoE grant DE-SC0007901. ML is partially supported by FAPESP and CNPq. This work made extensive use of the NASA Astrophysics Data System and [arXiv.org](http://arxiv.org) preprint server.

Funding for the DES Projects has been provided by the U.S. Department of Energy, the U.S. National Science Foundation, the Ministry of Science and Education of Spain, the Science and Technology Facilities Council of the United Kingdom, the Higher Education Funding Council for England, the National Center for Supercomputing Applications at the University of Illinois at Urbana-Champaign, the Kavli Institute of Cosmological Physics at the University of Chicago, the Center for Cosmology and Astro-Particle Physics at the Ohio State University, the Mitchell Institute for Fundamental Physics and Astronomy at Texas A&M University, Financiadora de Estudos e Projetos, Fundação Carlos Chagas Filho de Amparo à Pesquisa do Estado do Rio de Janeiro, Conselho Nacional de Desenvolvimento Científico e Tecnológico and the Ministério da Ciência e Tec-

nologia, the Deutsche Forschungsgemeinschaft and the Collaborating Institutions in the Dark Energy Survey.

The DES data management system is supported by the National Science Foundation under Grant Number AST-1138766. The DES participants from Spanish institutions are partially supported by MINECO under grants AYA2012-39559, ESP2013-48274, FPA2013-47986, and Centro de Excelencia Severo Ochoa SEV-2012-0234, some of which include ERDF funds from the European Union.

The Collaborating Institutions are Argonne National Laboratory, the University of California at Santa Cruz, the University of Cambridge, Centro de Investigaciones Energeticas, Medioambientales y Tecnologicas-Madrid, the University of Chicago, University College London, the DES-Brazil Consortium, the Eidgenössische Technische Hochschule (ETH) Zürich, Fermi National Accelerator Laboratory, the University of Edinburgh, the University of Illinois at Urbana-Champaign, the Institut de Ciències de l'Espai (IEEC/CSIC), the Institut de Física d'Altes Energies, Lawrence Berkeley National Laboratory, the Ludwig-Maximilians Universität and the associated Excellence Cluster Universe, the University of Michigan, the National Optical Astronomy Observatory, the University of Nottingham, The Ohio State University, the University of Pennsylvania, the University of Portsmouth, SLAC National Accelerator Laboratory, Stanford University, the University of Sussex, and Texas A&M University.

This paper is Fermilab publication FERMILAB-PUB-15-303-AE and DES publication DES-2015-0061. This paper has gone through internal review by the DES collaboration.

APPENDIX A: ALTERNATIVE E- AND B-MODE STATISTICS

In this appendix we consider alternative statistics of the shear field, verifying that our conclusions above, especially that the B-modes are consistent with zero, do not depend on the choice of statistic. These alternative statistics include the band-powers of Becker & Rozo (2014) and power spectra band-powers estimated with `PolSpice`¹⁶ (Szapudi et al. 2000; Chon et al. 2004).

A1 Band-powers

The band-powers of Becker & Rozo (2014) use the methods of Becker (2013) to estimate Fourier space band-powers directly from linear combinations of the real-space two-point functions. The final band-power estimates can be computed from the underlying E-mode power spectrum as

$$E = \int \frac{d \ln \ell \ell^2}{2\pi} C_{EE}(\ell) W_+(\ell) \quad (\text{A1})$$

where $W_+(\ell)$ is the band-power window function computed from the coefficients $\{f_{+i}, f_{-i}\}$ in Eqs. 3 & 4. See Becker & Rozo (2014) for more details. The optimal computation of the band-powers requires computing the effective radial bin window functions of the shear correlation function points.

¹⁶ <http://www2.iap.fr/users/hivon/software/PolSpice/>

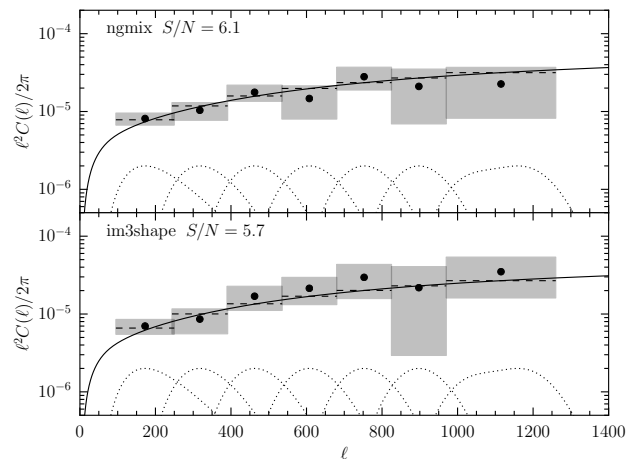


Figure A1. Band-powers in DES SV data for NGMIX (top) and IM3SHAPE (bottom). The error bars indicated by the grey bands are calculated from the simulation realizations using the shape noise appropriate for each catalog. The dotted lines show the band-power window functions $W_+(\ell)$ scaled so that their peak values are 2×10^{-6} . The solid line is the prediction for the shear power spectrum for the flat, Λ CDM model given above. The dashed line shows the integral of the band-power window functions over the shear power spectrum.

Instead in this work we just use the geometric approximation to the bin window functions to compute the amplitudes $\{f_{+i}, f_{-i}\}$. This procedure means that the band-powers do not separate E- and B-modes as well as they could in principle. However, when comparing to a fiducial cosmological model below, we do compute the band-power window function using estimates of radial bin window functions from the data. These window functions are computed via interpolating the weighted counts in each radial bin of the estimated shear two-point function. We have compared the results of this procedure for computing the window functions to estimates of the window functions from counts in finer bins. We find unsurprisingly that the bin window functions are quite smooth and thus the interpolation is accurate enough for our purpose.

A2 Spherical Harmonic Power Spectrum

The cosmic shear power spectrum can also be estimated in spherical harmonic space. For this purpose, we use the `PolSpice` (Szapudi et al. 2000; Chon et al. 2004) code together with the `HEALPix` (Górski et al. 2005) package. `PolSpice` is based on the fast correlation function approach described in Szapudi et al. (2000) and Chon et al. (2004). This algorithm first calculates pseudo- C_ℓ 's from pixelised and masked galaxy ellipticity maps which are then transformed to the correlation function. The real space correlation function is corrected for finite survey effects and inverted to obtain the full-sky power spectrum, removing E-to B-mode leakage in the mean. Incomplete sky coverage implies that the inversion can only be performed on angular scales for which the correlation function can be estimated and it further introduces Fourier ringing in the inversion process, which can be reduced by apodizing the correlation function. Both the apodization and finite integra-

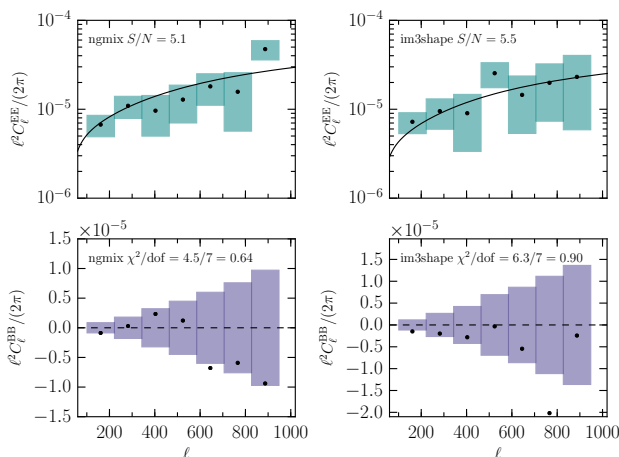


Figure A2. Spherical harmonic shear power spectrum estimated using `PolSpice`. The left and right panels correspond to the NGMIX and IM3SHAPE catalogs, respectively. The top and bottom panels show the E- and B-modes, respectively. The measurement uncertainties are estimated using the mock catalogs. The black solid lines show the predictions for the flat, Λ CDM model given above. Note that the theoretical prediction has been convolved with the `PolSpice` kernels, which relate the true to measured power spectra. The S/N values for the E-modes are computed as outlined in Section 4.1 and the χ^2 values for the B-modes indicate consistency with zero. The reported values take into account correlations between the band-powers.

tion range introduce kernels which relate the power spectra measured by `PolSpice` to the underlying true power spectra. These kernels can be computed for a given apodization scheme and integration range and can therefore be corrected for when comparing measurement to theory (for details see Chon et al. 2004). For our analysis, we pixelise the galaxy ellipticities onto a `HEALPix` pixelisation of the sphere with a resolution of `Nside=1024`, where each pixel covers a solid angle of 11.8 arcmin^2 . In order to obtain a robust estimate of the shear field, we need to correct for multiplicative bias in the measured ellipticities. Since the correction factors described in Sections 2.1 and 2.2 are noisy estimates of the true corrections, we determine the mean sensitivity or multiplicative bias correction for our galaxy sample and apply this mean correction to the pixelised maps. Additionally, we apply the DES SV LSS mask (Crocce et al. in preparation) to our maps in order to restrict to regions deeper than `MAG_I_AUTO = 22.5`. For the power spectrum measurement, we limit all integrations to scales smaller than $\theta_{\text{max}} = 15$ degrees and we apodize the correlation function with a Gaussian window of $\theta_{\text{FWHM}} = 10$ degrees. Finally, we compress the power spectra into 7 band-powers with `PolSpice` band-power kernels.

The noise power spectrum needs to be computed from simulations. In order to produce noise only maps, we remove correlations in the input maps by rotating each galaxy shear by a random angle. We then estimate the noise power spectrum as the mean of the power spectra of 100 such random realizations. This procedure yields shape noise estimates consistent with $C_{\ell,SN} = \frac{\sigma_\epsilon^2}{n_{\text{pix}}}$ where σ_ϵ^2 is the variance of either component of the mean ellipticity per pixel and n_{pix} is the number density of `HEALPix` pixels; this suggests that

the ellipticity distribution of the galaxies is non-Gaussian and therefore the analytic estimate can only be applied after averaging the distribution over pixels. We test the pipeline using Gaussian field realizations and the mock catalogs.

A3 Results

Figure A1 shows the non-tomographic band-powers using the methods of Becker & Rozo (2014), their window functions as the dotted lines, and their error bars computed with the mock catalogs as the grey bands. We find a detection significance 6.1σ and 5.7σ for NGMIX and IM3SHAPE, respectively. These detection significances are similar to the real-space two-point functions. Finally, the solid line shows the expected shear power spectrum amplitude assuming the flat, Λ CDM model given above. The dashed line shows for each band-power the integral of the band-power window function over the shear power spectrum.

Figure A2 shows the results for the `PolSpice` statistics. We find a detection of cosmic shear of 5.1σ and 5.5σ for NGMIX and IM3SHAPE respectively for the `PolSpice` statistics. Note that the `PolSpice` statistics do not use as many high- ℓ modes as the real-space band-powers or the real-space correlation functions, so that one expects a lower detection significance. We also find that the B-modes are statistically consistent with zero for the `PolSpice` statistics.

APPENDIX B: VALIDATION OF THE MOCK CATALOGS

In this section we present validation tests on the mock catalogs. We first compare the shear correlation functions measured in the mock catalogs in tomographic bins with the theoretical expectation from the Takahashi et al. (2012) fitting function for the matter power spectrum. The result of this test is shown in Figure B1. We find that at high redshift the small-scale shear correlation functions are suppressed relative to the theoretical expectation. Note however that this numerical effect is below the scales where the two-point functions are being used for cosmological parameter estimation (see Table 2 of DES et al. 2015). Additionally, we only estimate the covariance of the two-point functions from the mock catalogs. Our covariance matrices from the mock catalogs agree well with the halo model computations at small-scales, indicating that the covariance is less sensitive to these numerical effects (see Sec. 5 for a quantitative comparison). Future work may require higher-resolution shear fields for covariance estimation.

APPENDIX C: DETAILED COVARIANCE MATRIX VALIDATION

In this section, we present further details of the validation of the covariance matrices, including our tomographic halo model computations and the comparison to the simulations. The halo model covariance was computed with the `CosmoLike` covariance module (see Eifler et al. 2014b and Krause et al. 2015 for details).

In the halo model, the covariance of tomographic shear

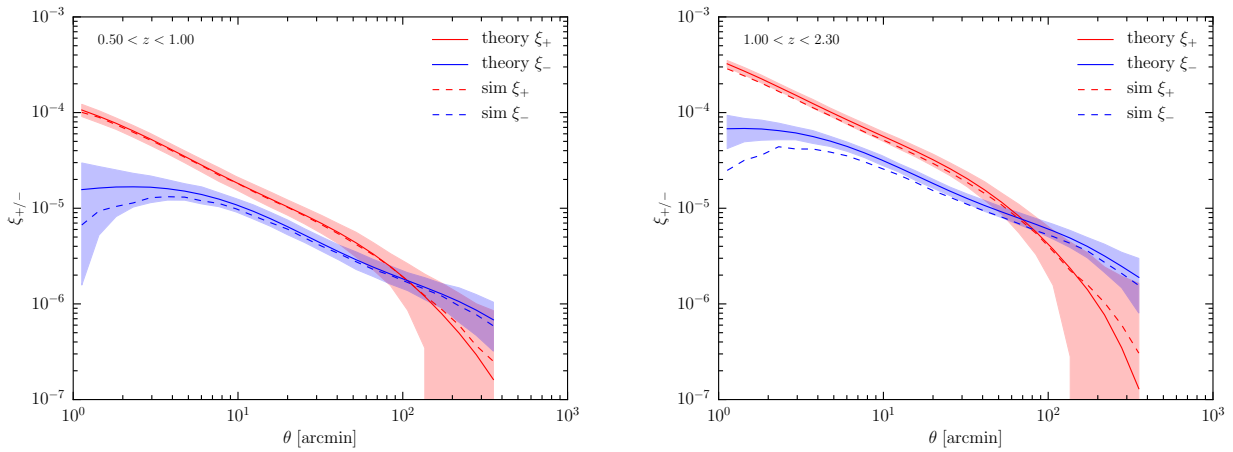


Figure B1. The shear correlation functions in the mock catalogs compared to the expected values from Takahashi et al. (2012) for the middle tomographic bin (left) and the upper tomographic bin (right). The solid lines show the theoretical expectation, the band shows the error bars including shape noise and the dashed line shows the mean from the mock catalogs. ξ_+ is in red and ξ_- is in blue.

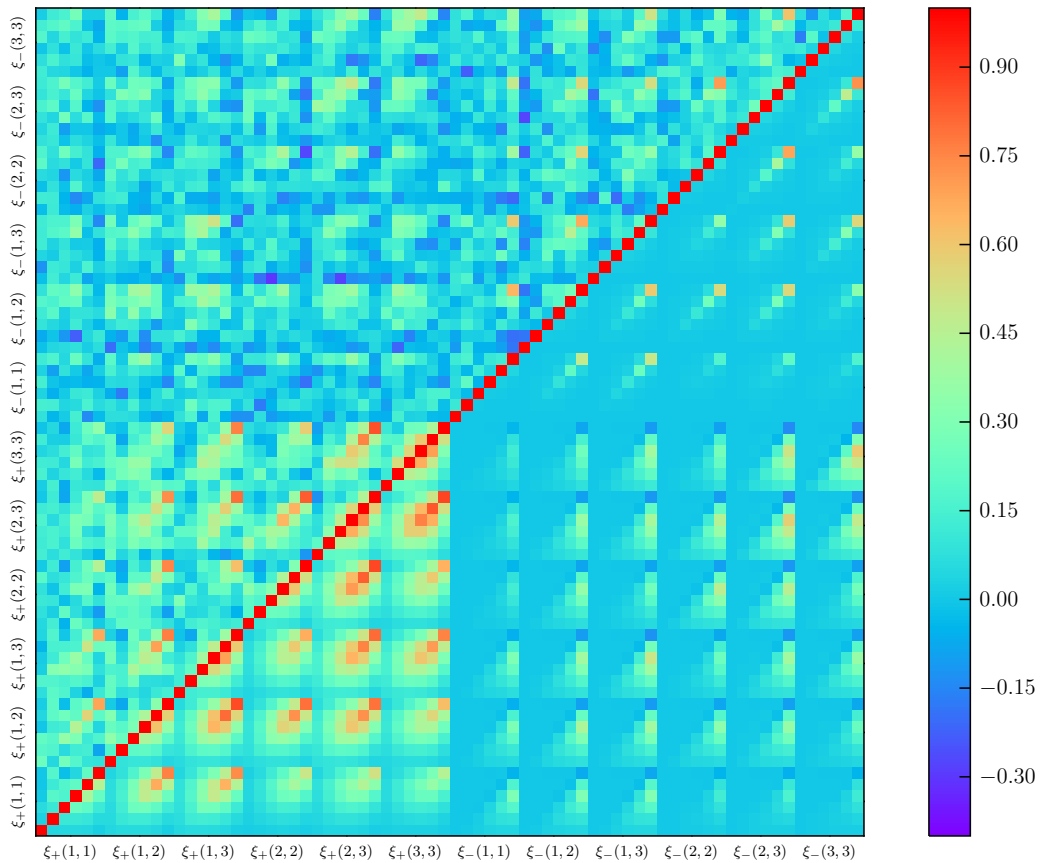


Figure C1. Comparison of the shear correlation function correlation matrix estimated from mock catalogs and calculated from the halo model. Figure 4 shows a subset, those for tomographic bin combinations (1,1), (1,3) and (3,3), of the covariance matrix elements shown in this figure. The correlation matrix from mock catalogs is on the upper-left and that from the halo model is on the lower-right.

$$\begin{aligned} \text{Cov}(C_{\kappa}^{ij}(l_1), C_{\kappa}^{kl}(l_2)) &= \frac{\delta_{l_1 l_2}}{2f_{\text{sky}} l_1 \Delta l_1} \left[\left(C_{\kappa}^{ik}(l_1) + \delta_{ik} \frac{\sigma_{\epsilon}^2}{2n^i} \right) \left(C_{\kappa}^{jl}(l_2) + \delta_{jl} \frac{\sigma_{\epsilon}^2}{2n^j} \right) + \left(C_{\kappa}^{il}(l_1) + \delta_{il} \frac{\sigma_{\epsilon}^2}{2n^i} \right) \left(C_{\kappa}^{jk}(l_2) + \delta_{jk} \frac{\sigma_{\epsilon}^2}{2n^j} \right) \right] \\ &+ \int_{|l| \in l_1} \frac{d^2 \mathbf{l}}{A(l_1)} \int_{|l'| \in l_2} \frac{d^2 \mathbf{l}'}{A(l_2)} \left[\frac{1}{\Omega_s} T_{\kappa,0}^{ijkl}(\mathbf{l}, -\mathbf{l}', -\mathbf{l}') + T_{\kappa,\text{HSV}}^{ijkl}(\mathbf{l}, -\mathbf{l}', -\mathbf{l}') \right], \end{aligned} \quad (\text{C1})$$

with n^i the number of source galaxies in tomography bin i , σ_{ϵ} the ellipticity dispersion, $A(l_i) = \int_{|l| \in l_i} d^2 \mathbf{l} \approx 2\pi l_i \Delta l_i$ the integration area associated with a power spectrum bin centered at l_i and width Δl_i , and $T_{\kappa,0}$ and $T_{\kappa,\text{HSV}}$ the convergence trispectrum in the absence of finite volume effects

and the halo sample variance contribution to the trispectrum (Sato et al. 2009; Takada & Hu 2013). Our halo model implementation for these terms is described in Eifler et al. (2014a).

The covariance of angular shear correlation functions is then given by

$$\text{Cov}(\xi_{\pm}^{ij}(\theta_1), \xi_{\pm}^{kl}(\theta_2)) = \int \frac{dl}{2\pi} l J_{0/4}(l\theta_1) \int \frac{dl'}{2\pi} l' J_{0/4}(l'\theta_2) \text{Cov}(C_{\kappa}^{ij}(l_1), C_{\kappa}^{kl}(l_2)) \quad (\text{C2})$$

where we use the results of Joachimi et al. (2008) to simplify the calculation of the Gaussian part of the covariance.

Figure C1 shows the full tomographic correlation matrix, comparing the halo model on the lower-right and the mock catalogs on the upper-left. The overall structure of the covariance matrices is similar in both computations, but the mock catalogs exhibit more noise in the off-diagonal components.

APPENDIX D: ADDITIONAL TWO-POINT NULL TESTS OF ξ_{-}

We have repeated an identical analysis for ξ_{-} to that described in Sec. 6.3 for ξ_{+} . We show the results of the tests for IM3SHAPE in Fig. D1 and for NGMIX in Fig. D2. Qualitatively, comparing to Figs. 9 & 10, there is an indication that some of the larger deviations in the figures for ξ_{+} may be due to additive systematic errors. For example, there is an offset in the difference of ξ_{+} based on values of airmass at the 2σ level that disappears for ξ_{-} . The corresponding χ^2 and difference values are given in Table D1. There are no significant indications of systematic errors in these null tests for ξ_{-} , though this may simply be due to the poorer constraining power of ξ_{-} .

REFERENCES

- Albrecht A. et al., 2009, arXiv:astro-ph/0901.0721
 Albrecht A. et al., 2006, arXiv:astro-ph/0609591
 Bacon D. J., Refregier A. R., Ellis R. S., 2000, MNRAS, 318, 625
 Bartelmann M., 2010, Class. Quant. Grav., 27, 233001
 Becker M. R., 2013, MNRAS, 435, 1547
 Becker M. R., Rozo E., 2014, arXiv:astro-ph/1412.3851
 Bonnett C., 2015, Monthly Notices of the Royal Astronomical Society, 449, 1043

- Bonnett et al., 2015, in preparation
 Chon G., Challinor A., Prunet S., Hivon E., Szapudi I., 2004, MNRAS, 350, 914
 Cooray A., Hu W., 2001, ApJ, 554, 56
 Crittenden R. G., Natarajan P., Pen U.-L., Theuns T., 2002, ApJ, 568, 20
 Crocce M., Pueblas S., Scoccimarro R., 2006, MNRAS, 373, 369
 DES et al., 2015, in preparation
 Desai S. et al., 2012, ApJ, 757, 83
 Diehl H. T., 2012, in Physics Procedia, Vol. 37, Proceedings of the 2nd International Conference on Technology and Instrumentation in Particle Physics (TIPP 2011), pp. 1332 – 1340, proceedings of the 2nd International Conference on Technology and Instrumentation in Particle Physics (TIPP 2011)
 Dodelson S., Schneider M. D., 2013, Phys. Rev. D, 88, 063537
 Eifler T., Krause E., Dodelson S., Zentner A., Hearin A., Gnedin N., 2014a, arXiv:astro-ph/1405.7423
 Eifler T., Krause E., Schneider P., Honscheid K., 2014b, MNRAS, 440, 1379
 Flaugher B. et al., 2015, arXiv:astro-ph/1504.02900
 Flaugher B. L. et al., 2012, in Society of Photo-Optical Instrumentation Engineers (SPIE) Conference Series, Vol. 8446, Society of Photo-Optical Instrumentation Engineers (SPIE) Conference Series, p. 11
 Górski K. M., Hivon E., Banday A. J., Wandelt B. D., Hansen F. K., Reinecke M., Bartelmann M., 2005, ApJ, 622, 759
 Graff P., Feroz F., 2013, SkyNet: Neural network training tool for machine learning in astronomy. Astrophysics Source Code Library
 Hartlap J., Simon P., Schneider P., 2007, A&A, 464, 399
 Heitmann K., Lawrence E., Kwan J., Habib S., Higdon D., 2014, ApJ, 780, 111
 Heymans C. et al., 2013, MNRAS, 432, 2433
 Hilbert S., Hartlap J., White S. D. M., Schneider P., 2009, A&A, 499, 31

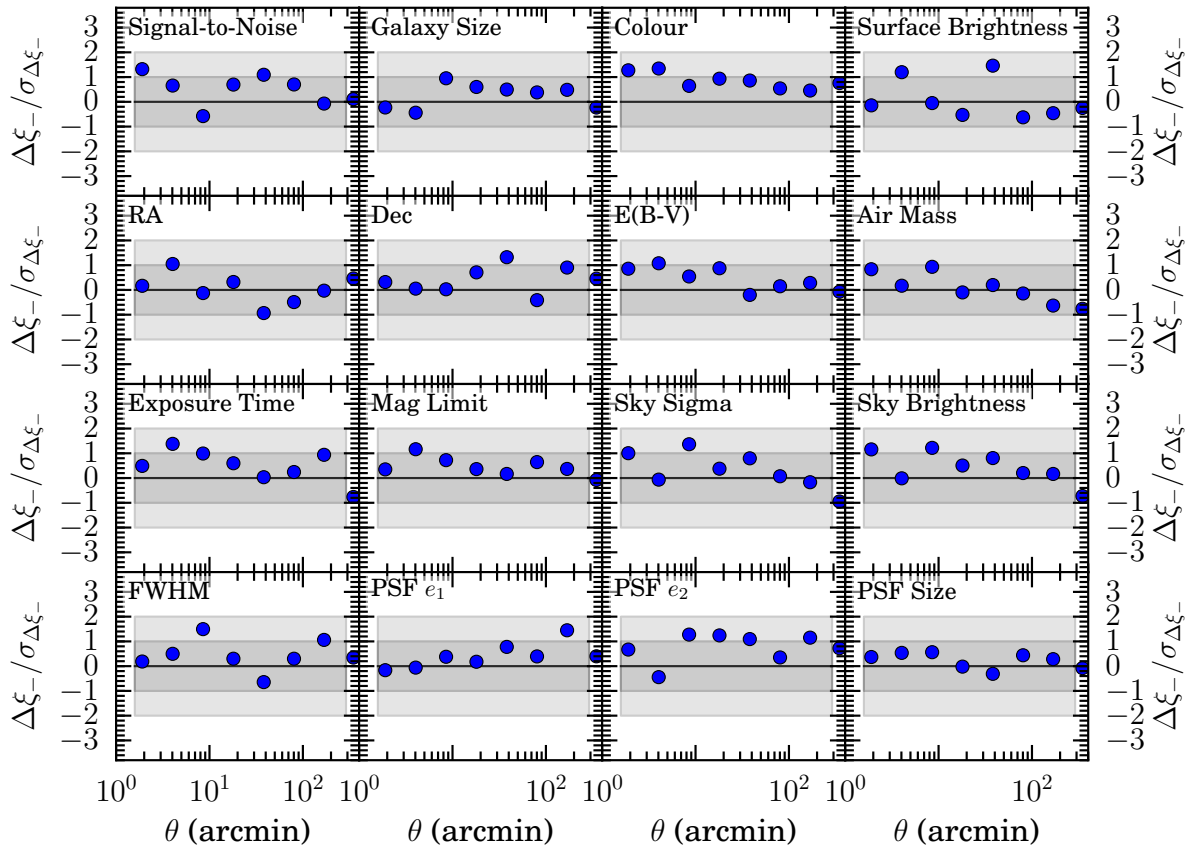


Figure D1. Null tests for the NGMIX two point correlation function based on a variety of catalog and survey properties as described in Table 1. See Fig. 9 for details.

Property	χ^2 [d.o.f. = 8] NGMIX (IM3SHAPE)	$\Delta\xi_-/\sigma(\xi_-)$ NGMIX (IM3SHAPE)	Description
Signal-to-Noise	5.8 (1.8)	-0.07 (0.03)	Signal-to-noise of galaxy detection
Galaxy Size	2.5 (5.0)	-0.23 (-0.35)	Galaxy size (deconvolved with PSF)
Galaxy Colour	7.1 (3.8)	-0.3 (0.04)	$g - z$ colour
Surface Brightness	4.4 (5.2)	-0.04 (-0.06)	Galaxy surface brightness
RA	2.9 (3.0)	0.06 (-0.22)	Galaxy right ascension
Dec	4.9 (3.5)	-0.35 (-0.37)	Galaxy declination
E(B-V)	2.8 (4.9)	-0.22 (-0.02)	Mean extinction
Air Mass	2.7 (3.4)	-0.01 (-0.08)	Mean r -band air mass
Exposure Time	4.5 (2.5)	-0.35 (0.0)	Mean total r -band exposure time
Mag. Limit	2.2 (3.3)	-0.29 (-0.43)	Mean r -band limiting magnitude
Sky Sigma	3.8 (5.6)	-0.21 (-0.3)	Mean r -band RMS sky brightness
Sky Brightness	4.0 (6.2)	-0.27 (-0.42)	Mean r -band sky brightness
FWHM	4.1 (4.5)	-0.2 (-0.08)	Mean r -band PSF FWHM
PSF e_1	2.7 (7.9)	-0.37 (-0.55)	Galaxy PSF e_1
PSF e_2	6.8 (5.8)	-0.5 (-0.33)	Galaxy PSF e_2
PSF Size	1.2 (3.8)	-0.08 (-0.1)	Galaxy PSF size

Table D1. Summary of null tests for NGMIX and IM3SHAPE. Results for NGMIX and IM3SHAPE are given as NGMIX (IM3SHAPE). The χ^2 values are given for the differences between the two-point correlation function calculated from galaxies that fall within one of two bins in each catalog or survey property. Also shown is the magnitude of the difference relative to the 1σ error of the measurement of ξ_- on the full sample.

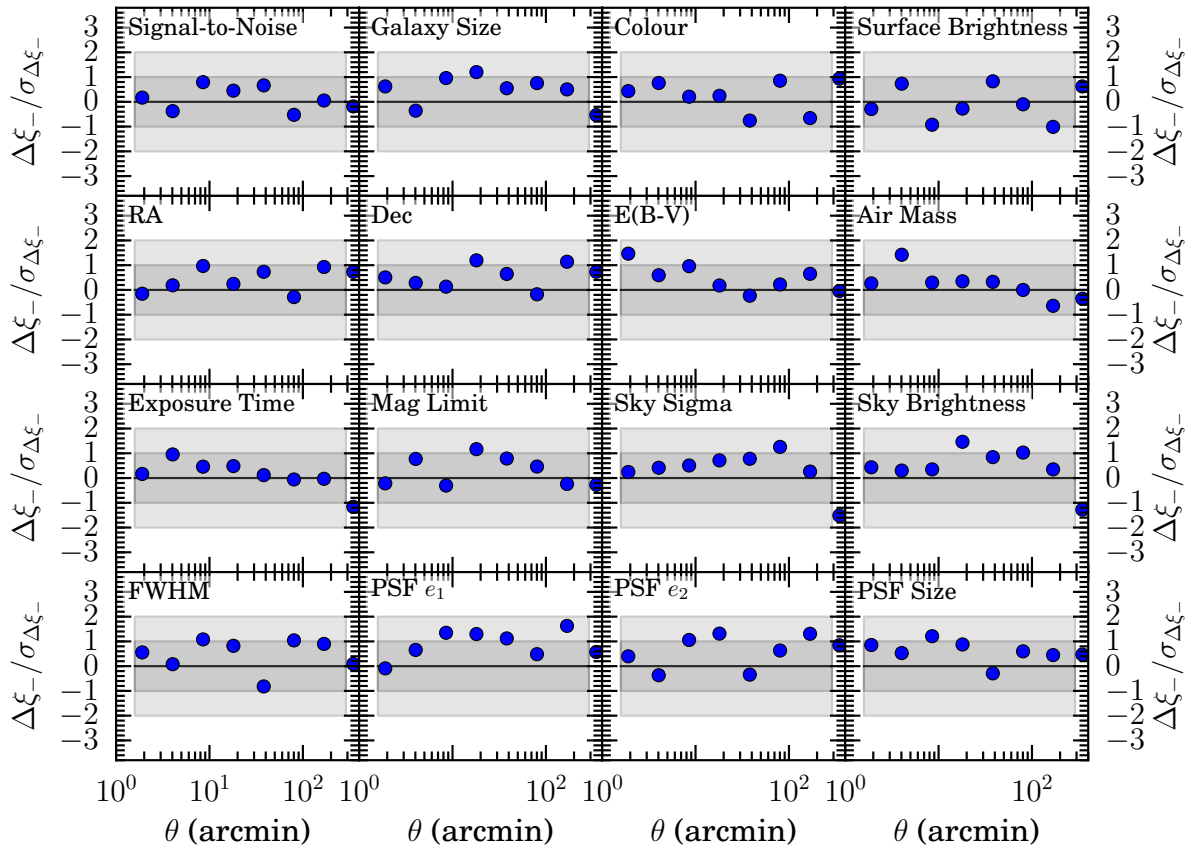


Figure D2. Null tests for the IM3SHAPE two point correlation function based on a variety of catalog and survey properties as described in Table 1. See Fig. 9 for details.

- Hogg D. W., Lang D., 2013, *PASP*, 125, 719
Honscheid K. et al., 2012, in *Society of Photo-Optical Instrumentation Engineers (SPIE) Conference Series*, Vol. 8451, Society of Photo-Optical Instrumentation Engineers (SPIE) Conference Series, p. 12
Hu W., Jain B., 2004, *Phys. Rev. D*, 70, 043009
Hu W., White M., 2001, *ApJ*, 554, 67
Huff E. M., Eifler T., Hirata C. M., Mandelbaum R., Schlegel D., Seljak U., 2014, *MNRAS*, 440, 1322
Jarvis M., Bernstein G., Jain B., 2004, *MNRAS*, 352, 338
Jarvis et al., 2015, in preparation
Jee M. J., Tyson J. A., Schneider M. D., Wittman D., Schmidt S., Hilbert S., 2013, *ApJ*, 765, 74
Joachimi B., Schneider P., Eifler T., 2008, *A&A*, 477, 43
Kacprzak T., Zuntz J., Rowe B., Bridle S., Refregier A., Amara A., Voigt L., Hirsch M., 2012, *MNRAS*, 427, 2711
Kaiser N., 1992, *ApJ*, 388, 272
Kaiser N., Wilson G., Luppino G. A., 2000, *arXiv:astro-ph/0003338*
Kilbinger M., 2014, *arXiv:astro-ph/1411.0115*
Kilbinger M. et al., 2013, *MNRAS*, 430, 2200
Kirk D. et al., 2015, *arXiv:astro-ph/1504.05465*
Krause E., Eifler T., Blazek J., 2015, *arXiv:astro-ph/1506.08730*
Krause E., Hirata C. M., 2010, *A&A*, 523, A28
Leistedt et al., 2015, in preparation
Lewis A., Bridle S., 2002, *Phys. Rev.*, D66, 103511
Lin H. et al., 2012, *ApJ*, 761, 15
Mandelbaum R. et al., 2014, *ApJS*, 212, 5
Miller L. et al., 2013, *MNRAS*, 429, 2858
Miller L., Kitching T. D., Heymans C., Heavens A. F., van Waerbeke L., 2007, *MNRAS*, 382, 315
Norberg P., Baugh C. M., Gaztañaga E., Croton D. J., 2009, *MNRAS*, 396, 19
Peacock J., Schneider P., 2006, *The Messenger*, 125, 48
Pedregosa F. et al., 2011, *Journal of Machine Learning Research*, 12, 2825
Refregier A., Kacprzak T., Amara A., Bridle S., Rowe B., 2012, *MNRAS*, 425, 1951
Sánchez C. et al., 2014, *MNRAS*, 445, 1482
Sato M., Hamana T., Takahashi R., Takada M., Yoshida N., Matsubara T., Sugiyama N., 2009, *ApJ*, 701, 945
Schneider P., Eifler T., Krause E., 2010, *A&A*, 520, A116
Schneider P., Kilbinger M., 2007, *A&A*, 462, 841
Schneider P., Seitz C., 1995, *A&A*, 294, 411
Schneider P., van Waerbeke L., Jain B., Kruse G., 1998, *MNRAS*, 296, 873
Seljak U., 1998, *ApJ*, 506, 64
Sheldon E. S., 2014, *MNRAS*, 444, L25
Springel V., 2005, *MNRAS*, 364, 1105
Szapudi I., Prunet S., Pogogyan D., Szalay A. S., Bond J. R., 2000, *arXiv:astro-ph/0010256*
Takada M., Hu W., 2013, *Phys. Rev. D*, 87, 123504
Takahashi R., Sato M., Nishimichi T., Taruya A., Oguri

- M., 2012, *ApJ*, 761, 152
- Troxel M. A., Ishak M., 2015, *Phys. Rep.*, 558, 1
- van Waerbeke L., et al., 2000, *Astron. Astrophys.*, 358, 30
- Weinberg D. H., Mortonson M. J., Eisenstein D. J., Hirata C., Riess A. G., Rozo E., 2013, *Phys. Rep.*, 530, 87
- Wittman D. M., Tyson J. A., Kirkman D., Dell’Antonio I., Bernstein G., 2000, *Nature*, 405, 143
- Zuntz J., Kacprzak T., Voigt L., Hirsch M., Rowe B., Bridle S., 2013, *MNRAS*, 434, 1604
- Zuntz J. et al., 2014, arXiv:astro-ph/1409.3409
- ¹ Department of Physics, Stanford University, 382 Via Pueblo Mall, Stanford, CA 94305, USA
- ² Kavli Institute for Particle Astrophysics & Cosmology, P. O. Box 2450, Stanford University, Stanford, CA 94305, USA
- ³ Jodrell Bank Center for Astrophysics, School of Physics and Astronomy, University of Manchester, Oxford Road, Manchester, M13 9PL, UK
- ⁴ Department of Physics and Astronomy, University of Pennsylvania, Philadelphia, PA 19104, USA
- ⁵ Jet Propulsion Laboratory, California Institute of Technology, 4800 Oak Grove Dr., Pasadena, CA 91109, USA
- ⁶ Max Planck Institute for Extraterrestrial Physics, Giessenbachstrasse, 85748 Garching, Germany
- ⁷ Universitäts-Sternwarte, Fakultät für Physik, Ludwig-Maximilians Universität München, Scheinerstr. 1, 81679 München, Germany
- ⁸ Department of Physics, ETH Zurich, Wolfgang-Pauli-Strasse 16, CH-8093 Zurich, Switzerland
- ⁹ Institute of Cosmology & Gravitation, University of Portsmouth, Portsmouth, PO1 3FX, UK
- ¹⁰ Institut de Física d’Altes Energies, Universitat Autònoma de Barcelona, E-08193 Bellaterra, Barcelona, Spain
- ¹¹ Fermi National Accelerator Laboratory, P. O. Box 500, Batavia, IL 60510, USA
- ¹² Kavli Institute for Cosmological Physics, University of Chicago, Chicago, IL 60637, USA
- ¹³ Department of Physics, University of Michigan, Ann Arbor, MI 48109, USA
- ¹⁴ Department of Astronomy, University of Michigan, Ann Arbor, MI 48109, USA
- ¹⁵ Institut de Ciències de l’Espai, IEEC-CSIC, Campus UAB, Carrer de Can Magrans, s/n, 08193 Bellaterra, Barcelona, Spain
- ¹⁶ Department of Physics & Astronomy, University College London, Gower Street, London, WC1E 6BT, UK
- ¹⁷ SLAC National Accelerator Laboratory, Menlo Park, CA 94025, USA
- ¹⁸ Korea Astronomy and Space Science Institute, Yuseong-gu, Daejeon, 305-348, Korea
- ¹⁹ Department of Physics, The Ohio State University, Columbus, OH 43210, USA
- ²⁰ Brookhaven National Laboratory, Bldg 510, Upton, NY 11973, USA
- ²¹ Cerro Tololo Inter-American Observatory, National Optical Astronomy Observatory, Casilla 603, La Serena, Chile
- ²² Department of Astrophysical Sciences, Princeton University, Peyton Hall, Princeton, NJ 08544, USA
- ²³ Institute of Astronomy, University of Cambridge, Madingley Road, Cambridge CB3 0HA, UK
- ²⁴ Kavli Institute for Cosmology, University of Cambridge, Madingley Road, Cambridge CB3 0HA, UK
- ²⁵ CNRS, UMR 7095, Institut d’Astrophysique de Paris, F-75014, Paris, France
- ²⁶ Sorbonne Universités, UPMC Univ Paris 06, UMR 7095, Institut d’Astrophysique de Paris, F-75014, Paris, France
- ²⁷ Laboratório Interinstitucional de e-Astronomia - LIneA, Rua Gal. José Cristino 77, Rio de Janeiro, RJ - 20921-400, Brazil
- ²⁸ Observatório Nacional, Rua Gal. José Cristino 77, Rio de Janeiro, RJ - 20921-400, Brazil
- ²⁹ Department of Astronomy, University of Illinois, 1002 W. Green Street, Urbana, IL 61801, USA
- ³⁰ National Center for Supercomputing Applications, 1205 West Clark St., Urbana, IL 61801, USA
- ³¹ George P. and Cynthia Woods Mitchell Institute for Fundamental Physics and Astronomy, and Department of Physics and Astronomy, Texas A&M University, College Station, TX 77843, USA
- ³² Excellence Cluster Universe, Boltzmannstr. 2, 85748 Garching, Germany
- ³³ Faculty of Physics, Ludwig-Maximilians University, Scheinerstr. 1, 81679 Munich, Germany
- ³⁴ Center for Cosmology and Astro-Particle Physics, The Ohio State University, Columbus, OH 43210, USA
- ³⁵ Australian Astronomical Observatory, North Ryde, NSW 2113, Australia
- ³⁶ Departamento de Física Matemática, Instituto de Física, Universidade de São Paulo, CP 66318, CEP 05314-970 São Paulo, Brazil
- ³⁷ Department of Astronomy, The Ohio State University, Columbus, OH 43210, USA
- ³⁸ Institució Catalana de Recerca i Estudis Avançats, E-08010 Barcelona, Spain
- ³⁹ Department of Physics and Astronomy, Pevensey Building, University of Sussex, Brighton, BN1 9QH, UK
- ⁴⁰ Centro de Investigaciones Energéticas, Medioambientales y Tecnológicas (CIEMAT), Madrid, Spain
- ⁴¹ Department of Physics, University of Illinois, 1110 W. Green St., Urbana, IL 61801, USA
- ⁴² SEPnet, South East Physics Network, (www.sepnet.ac.uk)
- ⁴³ Argonne National Laboratory, 9700 South Cass Avenue, Lemont, IL 60439, USA

This paper has been typeset from a \TeX / \LaTeX file prepared by the author.